CHALMERS
UNIVERSITY OF TECHNOLOGY

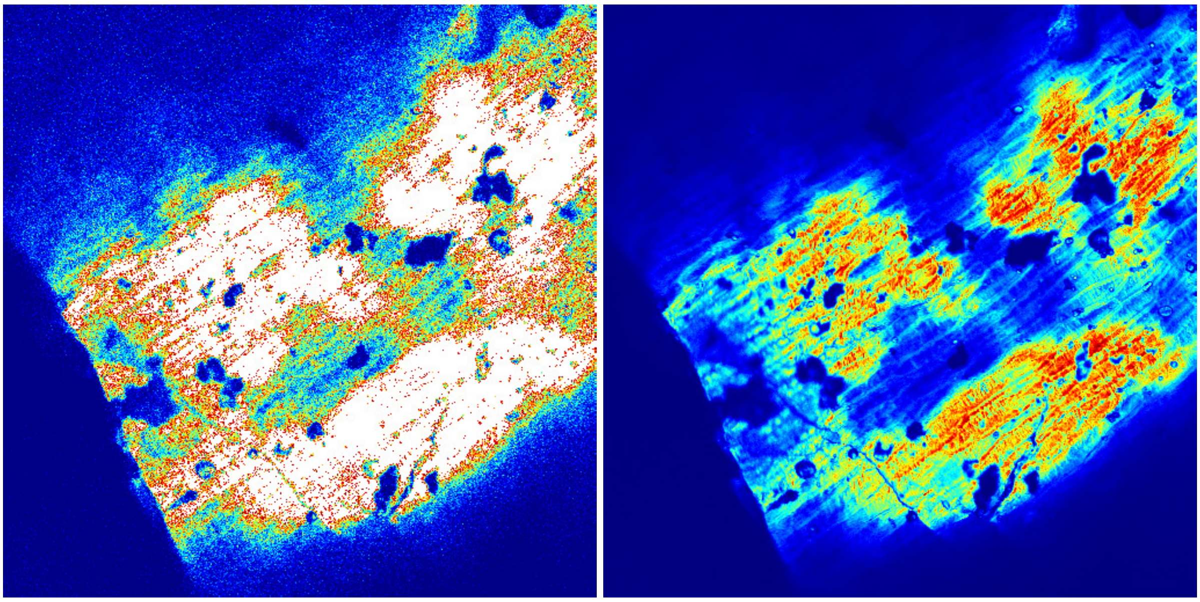

High Dynamic Range Image Processing of Confocal Laser Scanning Microscopy Data

Master's thesis in Engineering Mathematics and Computational Science

SEBASTIAN STÅHL

Mathematical Sciences
CHALMERS UNIVERSITY OF TECHNOLOGY
Gothenburg, Sweden 2016

High Dynamic Range Image Processing of Confocal Laser Scanning Microscopy Data

SEBASTIAN STÅHL

Department of Mathematical Sciences
Division of Mathematical Statistics
Chalmers University of Technology
Gothenburg, Sweden 2016

High Dynamic Range Image Processing of Confocal Laser Scanning Microscopy Data
SEBASTIAN STÅHL

Supervisor: Magnus Röding, SP Food and Bioscience, Soft Materials Science
Examiner: Mats Rudemo, Department of Mathematical Sciences, Division of Mathematical Statistics, Chalmers University of Technology

Department of Mathematical Sciences
Division of Mathematical Statistics
Chalmers University of Technology
SE-412 96 Gothenburg

Cover: Comparison between an image captured by the microscope (left) and the corresponding HDR image (right) generated for the same gain using the 3 parameter ML method. White pixels mark saturated (censored) areas. See Figure 4.25.

Abstract

All imaging sensors suffer from having a limited dynamic range, that is, the range of light intensities which can be accurately measured simultaneously, thus potentially limiting the amount of detail which can be captured in a single image. A method for generating high dynamic range (HDR) images from several regular low dynamic range (LDR) images captured using a photomultiplier tube imaging sensor for a confocal laser scanning microscope has been developed. This method uses data from all the available images in order to generate images which simulate an imaging sensor having unlimited dynamic range and simultaneously reduces the noise in the pixel intensity observations. The algorithm is based on solving a maximum likelihood estimation problem for censored data which yields estimates of the true, non-censored intensity values. The proposed method is demonstrated to generate HDR images containing details which were difficult or impossible to observe in the LDR images for several different kinds of samples. Furthermore, the method is validated by introducing artificial censoring in the original data and comparing the estimated intensities for different artificial thresholds to the observed intensities. The proposed method is shown to accurately predict the non-censored pixel values even for very low artificial thresholds (effectively simulating the behaviour of a sensor with a reduced dynamic range) which indicates that the method also accurately predicts the truly censored pixel intensities.

Acknowledgements

I would like to start off by thanking Magnus Röding, my supervisor at SP Food and Bioscience, for giving me the chance to work on this thesis and for his ideas, support and encouragement throughout the project. I would also like to thank Mats Rudemo, my supervisor and examiner at Chalmers, for his insightful input and suggestions during our meetings at his office. Lastly, I would like to thank all my colleagues at the department of Soft Materials Science at SP Food and Bioscience for welcoming me to the research group and making my stay there enjoyable.
Thanks also goes out to C3SE (www.c3se.chalmers.se) for enabling us to run computations on their computer cluster.

Sebastian Ståhl, Gothenburg, June 2016

Contents

List of Figures

List of Tables

List of Acronyms

A/D analog-to-digital.
AOTF acousto-optic tunable filter.
CDF cumulative distribution function.
CLSM confocal laser scanning microscopy.
CTF camera transfer function.
ENF excess noise factor.
HDR high dynamic range.
HyD hybrid detector.
LDR low dynamic range.
LS least squares.
ML maximum likelihood.
MLE maximum likelihood estimation.
PDF probability density function.
PMT photomultiplier tube.

1
Introduction

This section serves as an introduction to the problem with which this thesis is concerned. The section includes a short background and a summary of earlier related work as well as the aim and the delimitations of the project.

1.1 Background

Microscopy techniques are used to study many different phenomena in complex materials. In this project, we are concerned in particular with confocal laser scanning microscopy (CLSM). One general problem in *digital* microscopy, i.e. when the image is digitized using a digital light sensor, is that light sensors have limited dynamic range. Hence, the range of light intensities that the sensor can accurately measure is limited. This means that for a sample yielding both low and high signal intensities it might not be possible to capture the desirable amount of detail in a single image. The microscopist can therefore be forced to choose settings that give a high level of overall detail, but risk missing important details in areas which are comparatively very dark or very bright.

One way of solving the problem of limited dynamic range would be to, after the experiment, combine a number of low dynamic range (LDR) images into a single high dynamic range (HDR) image. Ultimately, the goal would be to produce the image which would have been obtained had the dynamic range of the sensor not been limited. This image would contain more information than any of the individual LDR images and thus provide a more accurate visual representation of the studied sample. A naive approach would be to capture a number of images using different levels of exposure and then simply merging the images, by for subsets of pixels choosing the pixel values from the image which for this particular area has the most appropriate dynamic range, forming a sort of patchwork. However, this approach has a number of drawbacks. An image created in this way will have jagged ”edges” where areas from two different images meet. Furthermore, an observed pixel intensity value is dependent on not only the ”inherent” brightness of the area comprising the pixel, which is a property of the material, but also on microscope settings and illumination conditions, which are independent of the sample as such. Therefore, it appears, an absolute, inherent measure of local optical properties of the material in a pixel, independent of the means of observation, cannot be obtained. In other words, if pixel A in this patchwork image has an intensity of 0.4 and pixel B has an intensity of 0.7 (on a grayscale where black is 0 and white is 1), you cannot conclude that pixel B is in reality brighter than pixel A since their signals are not measured under equal conditions. This approach would also only use data from a single observation per pixel even though several measurements exist (one for each image captured) and therefore would not utilize data very efficiently.

A better way of creating the HDR image would therefore be to acknowledge the fact that pixel intensities for a range of acquisition settings provide a wealth of information not attainable from a single LDR image. For each pixel, using all the available data from a set of LDR images should minimize the effect of noise and signal saturation and yield a more reliable model. In other words, we would like to estimate the effects of the variable input, i.e. the settings of the microscope, on the output, i.e. the observed pixel intensity. Statistically, this is a regression analysis problem, and an interpolation and extrapolation problem. The idea is that if we can express the relationship between input and output mathematically we can use this model to estimate the true intensities of an image. When this value is larger than the sensor's saturation level we are effectively circumventing the physical limitations of the sensor.

We emphasize the difference between the dynamic range of the detector and the dynamic range of the image *format*. The dynamic range of an image format is the number of representable grayscale values, i.e. 2^b where b is the *bit depth* and typically equal to 8, 12, or 16. However, this number carries no information concerning the highest and lowest *physical* intensities that can be represented in this range, which is rather a property of the sensor and referred to as the dynamic range of the sensor. The goal of this thesis is to obtain images simulating an increased dynamic range of the imaging sensor which will produce an image which might have an increased dynamic range. As such, the concept of an high dynamic range (HDR) image will denote an image simulating a high dynamic range imaging sensor, not just an image containing a large number of distinct intensity values.

1.2 Earlier related work

Methods for conducting HDR imaging in photography is a relatively well-explored area, see e.g. [2, 3, 4] . Work has also been conducted to develop HDR techniques in the area of optical microscopy [5, 6, 7]. In general these methods utilize a so-called camera transfer function (CTF) f, generally defined as

$$I_j = f(Q_j) \tag{1.1}$$

where I is the registered intensity and Q is the total incident radiant energy for pixel j. The CTF is typically a non-linear function which is estimated using the data contained in the LDR images. Linear CTFs have been used by e.g. [8] but are only appropriate when modelling the raw data (i.e. unprocessed data) produced by the image capturing device. One of the more straightforward ways of estimating f is to solve an optimization problem which has been done by e.g. [9] and [10]. The idea is to write eq. (1.1) on the form

$$I_{i,j} = f(x_j t_i + N_{i,j}) \tag{1.2}$$

where j is the pixel index as before, i denotes the image index, t_i is the exposure time for image i, x_j is the scene irradiance (radiant flux received by a surface per unit area) and $N_{i,j}$ is a noise term. The goal is then to model $N_{i,j}$ so that x_j can be estimated from a series of observations. Ideally, modelling of $N_{i,j}$ should be done by carefully examining the noise contribution of the different electrical components of the image capturing device. However, this turns out to be rather complicated to do in practice, which is why a more simple approach is generally used. For example, [9] model the noise $N_{i,j}$ as independent zero-mean Gaussian random variables with variances $\sigma_{i,j}$ and uses a ML approach. This optimization problem is solved iteratively and yields estimates of the CTF as well as the irradiance values x_j which can subsequently be used as pixel values in the HDR image estimation. More general theory for the CTFs can be found in [11] which lists a number of parametric equations for possible CTFs and in [12] which provides a detailed model for the space of both theoretical and practical CTFs.

When the CTF is known (i.e. it has already been estimated using e.g. the above outlined method), it can then be used along with a weighting function to determine the pixel value contribution of each LDR image towards the generated HDR image. The choice of weight function differs between different papers, for example [2] and [5] used the derivative of the CTF, [3] used a triangular function peaking at the center of the domain (at pixel value 0.5) whilst [9] used a Gaussian function. What all of these choices of weighting functions have in common is that they diminish the impact of pixel values close to the edges of the domain (i.e. pixel values close to either 0 or 1), instead favoring the pixel values closer to the middle of the range. The motivation behind the choice of these kinds of weighting functions is clear, namely that we would like to avoid using underexposed or overexposed pixels for the HDR composition as they contain less information than observations closer to the middle of the intensity domain.

If the generated HDR image is to be displayed on e.g. a computer monitor, the image has to undergo tone mapping before it can be properly displayed. Tone mapping is a process in which the large dynamic range of an image is mapped onto a smaller dynamic range. This is necessary since most monitors have a limited dynamic range of the intensity which they can accurately display, much like camera sensors have a limited dynamic range of intensities which they can accurately capture. In photography, it is common that a tone mapping used for this purpose utilizes models of the human visual system in order to obtain an image which resembles how the human eye would have processed the scene. However, in the case of CLSM this isn't useful as the images are supposed to first and foremost provide quantitative information and display that information accurately – not to create images which look appealing in a subjective sense.

When it comes to the subject of HDR acquisitions from CLSM images there is, to the best of our knowledge, no papers published on the subject. Thus, although there is inspiration to be found in the works related to photography and optical microscopy, the subject of this thesis is largely uncharted territory.

1.3 Aim

To develop and implement an HDR algorithm for image data obtained using a confocal laser scanning microscope with different sensor types.

1.4 Delimitations

The images used in this work will be captured using a limited number of different sensors. As such the main focus of the work will be to model these specific sensor types which could potentially limit the area of application of the produced models and algorithms. We also choose to neglect the impact of small movements of the sample during acquisition of images.

2

Theory

This section outlines the relevant theoretical background. First, an introduction to the CLSM technique is given, along with a description of the two sensor types that will be considered. Some relevant but non-essential mathematical theory can be found in Appendix C.

2.1 Confocal laser scanning microscopy

The main advantage of confocal microscopy over common optical microscopy is the pinhole, a spatial filter which eliminates light from sources outside the focal plane, hence increasing resolution and contrast. In order to measure the local intensities the microscope uses point scanning which is a procedure where a focused laser beam is run over the sample. The pattern which the beam follows as it moves over the sample is called a raster and usually goes one row at a time from top to bottom. The photons coming from the focal point enter the pinhole unobstructed whilst the photons coming from objects out-of-focus are spread out over a larger area. This means that the photons coming from an out-of-focus object which reach the sensor are only a fraction of the photons emitted from said object. The sensor produces a voltage which is a function of the number of incoming photons. As the laser beam moves along the raster the produced voltage will vary, resulting in an analog signal. The analog signal is converted by an analog-to-digital (A/D) converter which generate the pixel values which make up the generated image. [13, Ch. 13]

Another reason why CLSM is useful is because it requires no preparations (possibly apart from staining with fluorescent dyes) at the same time as it does very little damage to the sample. The latter is particularly important for the application of HDR imaging as the process requires capturing several images which means that the sample will be under exposure for an extended period of time. Long exposures typically lead to photobleaching, a process in which photochemical changes causes a dye to stop being fluorescent. Since a non-fluorescent molecule won't be detectable through the microscope this means that photobleaching will make the captured images darker over time. In other words, photobleaching will cause the image intensity to be time-dependent. The fundamental assumption of this thesis is that all images are captured under equal conditions, thus the experiments will be designed such that the effect of photobleaching is negligible.

2.1.1 Sensor types

This section will give a short description of the sensors used in the experiments.

2.1.1.1 Photomultiplier tube

The photomultiplier tube (PMT) operates as follows. When a photon reaches the sensor, the cathode absorbs the photon and consequently has a chance of emitting a free photoelectron. The chance that an electron is released due to the absorption of a photon is called the quantum efficiency which is a property of the sensor. Assuming that an electron is released at the cathode it is subsequently guided by an applied electric field through a number of dynodes. At each dynode every incoming electron which hit the dynode is multiplied, causing a non-deterministic number of secondary electrons to be emitted. When the electrons have passed the last dynode they are absorbed at the anode where the charge is measured, resulting in a pixel intensity value. [14]

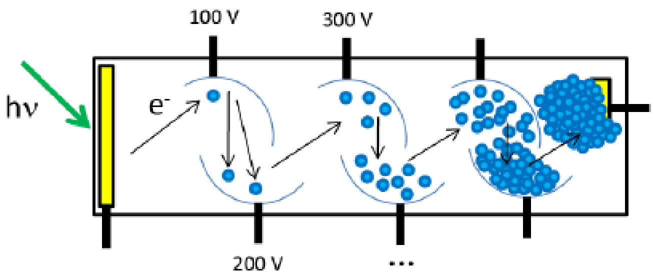

Figure 2.1: A conceptual visualization of the PMT. Image courtesy of [1].

The number of secondary electrons emitted by the dynode for each incoming electron is a random quantity. The gain of the PMT is defined as the total number of electrons collected at the anode due to a single electron emitted at the cathode. The gain of the PMT is thus a random variable where the expected gain is a function of the total voltage of the dynodes. Through the multiplication process occuring at the dynodes, additional noise is generated since all passing electrons will have the same chance of being multiplied at the dynodes. This noise can be expressed through the excess noise factor (ENF) F_e, defined as

$$F_e = \frac{\overline{M^2}}{\overline{M}^2} \tag{2.1}$$

where M is the gain (which is a random variable) and the bar $(\bar{\cdot})$ denotes the average of a quantity. For a PMT the ENF can be shown to be (equation (38) in [15])

$$F_e = 1 + \frac{\mathrm{Var}(\delta_1)}{\overline{\delta_1}^2} + \sum_{i=2}^{m} \frac{\mathrm{Var}(\delta_i)}{\overline{\delta_i}^2 \cdot \prod_{k=1}^{i-1} \overline{\delta_k}} \tag{2.2}$$

where δ_i is the emission of secondary electrons at dynode number i, m is the number of dynodes and $\mathrm{Var}(\cdot)$ is the variance operator. The voltage which produces the gain is typically equally distributed among the dynodes, although in some situations a higher voltage is applied at the first dynode (with all the subsequent dynodes having an equal voltage). One motivation for using a higher voltage at the first dynode can be found by looking at equation (2.2); all non-constant terms in the equation are inversely proportional to the average number of multiplications occurring at the first dynode. Increasing the voltage at the first dynode is thus typically the most efficient way of decreasing the noise generated through the multiplication process.

Since the electrons travelling through the tube can take different paths to reach the anode, they don't necessarily arrive there at the same time. This gives rise to an output pulse which has a relatively large width. The wider the output pulse the more difficult it will be to distinguish between individual events (signals). The fact that electrons take different paths also lead to some electrons missing the subsequent dynodes and they are thus not collected at the anode. This further increases the variability in the number of electrons registered at the anode for a single electron emission at the cathode.

PMTs suffer from a so-called dark current, created despite a lack of incoming photons, hence a low-amplitude signal is observed even if the device is operated in complete darkness. Consequently, a signal which is weaker than or in the same order as the dark current will be difficult to accurately detect. Effectively, the dark current puts a lower bound to the dynamic range of the PMT.

In the case of a PMT, the dynamic range is defined to be the ratio between the saturated signal and the background noise which can be measured in either volts or electrons. The available dynamic range of the PMT is usually of 5 to 7 orders of magnitude. If this dynamic range is greater than what can be represented by the desired bit depth, the signal has to undergo dynamic compression before it is stored digitally. This is done in one of two ways. Either a logarithmic amplifier is used to scale the signal after it has been registered at the anode or the PMT is operated in a compressed-output mode in which the signal is directly registered in compressed form [14].

2.1.1.2 Photon counting sensor

The sensor used for photon counting is a Leica hybrid detector (HyD) (Leica Microsystems, Wetzlar, Germany). The design of the sensor is as follows. A photon is absorbed at the photocathode which generates a free electron. The electron is accelerated in a vacuum at a voltage of 8 kV. It then hits the semiconductor material where the energy is first converted into approximately 1500 charge pairs. These pairs are subsequently amplified in a multiplication layer by a factor of about 100 after which the signal becomes a measurable pulse. The photon counting is done by thresholding the measured electrical pulses and classifying them as binary events [1].

One of the advantages of the HyD compared to the PMT is that the width of output pulses are reduced by a factor of about 20 (the pulse is about 1 ns for the HyD and around 20 ns for the PMT). The pulses are also typically more homogeneous as the variation of emitted secondary electrons are decreased. The design also reduces dark current-type noise as it eliminates the dark currents which arise in the PMT due to the secondary electrons which miss the dynodes [1].

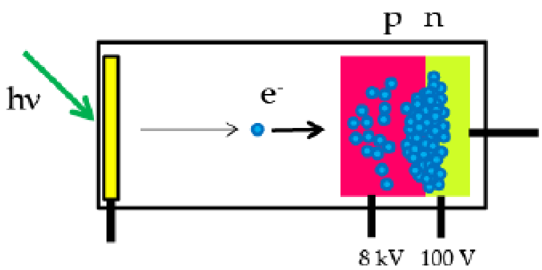

Figure 2.2: A conceptual visualization of the HyD. Image courtesy of [1].

2.1.2 Potential sources of noise in images

The dark current of a PMT, mentioned in section 2.1.1.1, and the noise introduced by the variation of the gain occurring at each dynode are sources of noise which depend on the hardware. The dark current is typically measured by the manufacturer of the microscope making it possible to make adjustments for or at least obtain an estimate of its influence. The statistical variation of gain occurring at the dynodes, however, is more difficult to model. Parts of this noise is the ENF which can be estimated using equation (2.2), but a more detailed analysis requires knowledge about the underlying statistical distribution which is discussed in section C.2.

If the sample were to move in space during the image acquisition this would introduce a variation between observations which could be classified as spatially varying noise. For the datasets considered in this thesis no such movements have been detected during visual inspection of the raw images. For all these datasets it is possible to identify a distinguishable object in one frame and then find the object to be located at the same pixel coordinates in both preceding and subsequent frames. As such it is reasonable to assume that if any such movements in space occur, the effects will have negligible impact on the final results of our processing. It should be noted that if the physical lengths corresponding to the size of a pixel were to change, e.g. by using a higher resolution for the same physical area or if a greater zoom was used, then these effects could potentially become large enough to affect the resulting images. This is important to keep in mind when setting up the microscopy for data acquisition.

The number of photons emitted from an object per time unit is a random quantity which often can be modelled by a Poisson process. This variation in the photon flux creates noise called photon shot noise. The influence of this noise source can often be limited by frame averaging, i.e. taking the average of multiple frames to create a single image where the effects of photon shot noise is reduced. In fact, the signal-to-noise ratio increases in proportion to the square root of the number of frames used in the averaging [13, Ch. 13]. It is thus one of the noise sources whose effect could potentially be reduced through an HDR composition which utilizes data from many images.

The A/D converter potentially introduces noise in the observations as the measured signal has to be (linearly) mapped to a limited number of intensity values. This number depends on the bit depth b, i.e. how many bits are used to store the image. Since the maximum number of distinct signal values which can be stored is equal to 2^b, there will in some situations be signals which are initially measured to have different values but stored as being equal due to the limited bit depth, generating so called truncation noise. In general, truncation noise approximately follows a normal distribution. Increasing the bit depth is the best way of decreasing this noise, which is often small in practice given that a sufficient bit depth is used.

Objects which lie outside the focal plane of the CLSM will in theory introduce noise in the captured images as some of the photons emitted by these objects will reach the sensor. As mentioned in section 2.1, the out-of-focus photons that reach the sensor are only a fraction of those received from the focal region and as such the contribution from this noise source is assumed to be small, which will be the case given that the pinhole width has been set at an appropriate level.

2.1.3 Mechanical adjustments of the microscope

For CLSM, there are several mechanical adjustments which can be made in order to change properties such as brightness and resolution of the generated image. In order to generate an HDR image it is important that the parameter settings used for acquiring the LDR images are identical except for a parameter controlling the intensity, which is varied by either controlling the emitted light or controlling the sensor sensitivity to light. As such it is assumed that parameters such as laser scan rate, electronic zoom factor, lens, resolution etc. remain constant throughout a series of images. To this end, the most interesting adjustments to study in our case are those which affect the image intensity. These include adjustments of the laser and gain/offset of the sensor in the case of a PMT.

An acousto-optic tunable filter (AOTF) can be used to select which wavelength is desired for a system having several laser wavelengths. The power level at which a laser operates (specified as a percentage of its full capacity) can be adjusted through the software connected to the microscope. In practice a laser is typically operated on a power level which lies far below its maximum power. The reason behind this is twofold. One reason is that the lifetime of the laser as well as some other parts of the microscope is shortened when the laser is operating at a high power level. The other reason is that you want to avoid causing damage to biological samples and minimize photobleaching. [13, Ch. 13]

The gain and offset of the PMT can be changed in order to adjust the light intensity of the images. The offset is an adjustment representing the addition of a fixed voltage (negative or positive) to the signal and should be set such that for a suitable background signal the sensor output is approximately 0 V. Once the offset has been set it's appropriate to adjust the gain (defined in section 2.1.1.1). Adjustments are typically made so that the intensities match the full dynamic range of the sensor. Normally the gain should be balanced such that there are as few underexposed pixels (value close to 0) and as few overexposed pixels (value close to 1) as possible [13, Ch. 13]. In our case, however, the gain will be varied such that some of the LDR images may have a large fraction of underexposed or overexposed pixels.

3

Methods

This section covers the methods used when developing and testing the modelling of the different sensor behaviours and the HDR acquisition. It also contains the experimental setup used to capture images, covered in section 3.1, as well as a list of the datasets used, section 3.2.

3.1 Method and materials for data acquisition

The microscope used to obtain the images is a Leica TCS SP5 (Leica Microsystems, Wetzlar, Germany). The laser is a 100 mW argon laser with emission maximum at 488 nm, operating at a power level of 25%. The laser beam passes through an AOTF which is used to control the laser/illumination intensity. Whenever the laser intensity of a dataset is presented it's in fact the percentage at which the AOTF is set which is given. The pinhole width was 53.1 μm with a zoom of 1.0 (i.e. no digital zoom).

The PMT used has a multialkali photocathode and consists of 9 dynode stages. The HyD sensor has a GaAsP photocathode.

3.2 Datasets

This section gives a list of the different datasets which have been acquired and analyzed for this thesis. Example images from some of the datasets can be found in Appendix B. Note that the omitted equipment and equipment settings specifications follow the settings outlined in (3.1).

1. *pc_1*: 250 images of a fixed, static sample (PUR foam) captured in succession using the photon counter sensor. Laser intensity was fixed at 16% for all images.

2. *pc_2*: 16 images of a fixed, static sample (PUR foam) captured using the photon counter sensor. The laser intensity for these images started at 2.5% and was increased in increments of 2.5% until 40% was reached (one image

was captured at each increment).

3. *pmt_1*: 250 images of a fixed, static sample (PUR foam) captured in succession using the PMT sensor. Gain was fixed at 893 V for all images.

4. *pmt_2*: 25 images of a fixed, static sample (PUR foam) captured using the PMT sensor. The gain for these images started at 50 V and was increased in increments of 50 V until 1250 V was reached (one image was captured at each increment).

5. *pmt_3*: 1312 images of a fixed, static sample (PUR Foam) captured using the PMT sensor. The gain for these images started at 0 V and was increased linearly until 1250 V was reached (one image was captured at each gain level).

6. *pmt_3_trunc*: a truncated version of the dataset *pmt_3* where the first 600 images are omitted (the gain used for these 600 images are so low that the raw images are very close to being completely dark). The first image of this dataset is captured using a gain of 571.13 V.

7. *pmt_4*: 2500 images of a fixed, static sample (PUR Foam) captured in succession using the PMT sensor. Gain was fixed at the same voltage for all images.

8. *wheat_bran*: 150 images of a fixed, static sample (wheat bran) captured in succession using the PMT sensor. The gain interval used was $[500, 800]$. The physical length is 1.516 μm (2x zoom) per pixel for both directions and the AOTF was set to 10 %.

9. *emmer*: 150 images of a fixed, static sample (emmer wheat) captured in succession using the PMT sensor. The gain interval used was $[500, 800]$. The physical length is 1.011 μm (3x zoom) per pixel for both directions and the AOTF was set to 10 %.

10. *toilet_paper*: 150 images of a fixed, static sample (toilet paper) captured in succession using the PMT sensor. The gain interval used was $[650, 1100]$. The physical length is 1.516 μm (2x zoom) per pixel for both directions and the AOTF was set to 20 %.

11. *lens_paper*: 150 images of a fixed, static sample (lens paper) captured in succession using the PMT sensor. The gain interval used was $[500, 800]$. The physical length is 1.516 μm (2x zoom) per pixel for both directions and the AOTF was set to 20 %.

12. *foam*: 150 images of a fixed, static sample (PUR foam) captured in succession using the PMT sensor. The gain interval used was $[600, 1000]$. The physical length is 3.033 μm (1x zoom) per pixel for both directions and the AOTF was set to 30 %.

Datasets 1-4: 1024x1024 resolution with a physical length of 1.5 μm per pixel in both directions. A 12 bit depth for the intensity values was used. The lens used was a HCX PL APO CS 10.0x0.40 DRY UV.

Datasets 5-7: 1024x1024 resolution with a physical length of 3 μm per pixel for both directions. A 16 bit depth for the intensity values was used. The objective used was a HCX PL FLUOTAR 5.0x0.15 DRY.

Datasets 8-12: 512x512 resolution with a 16 bit depth for the intensity values was used. The lens used was a HCX PL APO CS 10.0x0.40 DRY UV. The gain was increased linearly starting at the lower endpoint of the interval and finishing in the upper endpoint

3.3 Modelling of the sensors

3.3.1 The photon counter sensor

In order to correctly model the behavior of the measured image intensities it's useful to investigate the probability distribution which produces the intensity values. According to theory the observed intensities for a photon counting sensor should be Poisson distributed, although this assumption could sometimes fail in practice e.g. if there is too much electronic noise in the vicinity of the microscope. A first step in the modelling process is thus to investigate the assumption of an underlying Poisson distribution.

Qualitatively, the Poisson assumption can be investigated by comparing the observed samples (images) to generated samples coming from a Poisson distribution where λ is estimated from the observations. Quantitatively, the Poisson assumption can be investigated e.g. by checking the validity of eq. (C.2) for the observed samples.

Given that the Poisson assumption is valid, the next step is to model how the expected intensity λ in a given pixel varies as the laser intensity is adjusted. One way of doing this is to plot the observed intensity as a function of the laser intensity and try to find a curve which fits the observed data well. To this end several different functions such as polynomials of different degrees and exponential functions were tested. The best fit observed during this testing is given by a polynomial on the form

$$I_i = \alpha_i \cdot L^{\gamma_i} \tag{3.1}$$

where I is the observed intensity, i is the pixel index, L is the laser intensity and α and γ are model parameters. The parameters are fitted using regular LS.

With a bit-depth of 12 bits the photon counter has not been close to saturating. Thus, the main improvements which could be expected to be reached through an HDR image in the case of a photon counter is to increase the detail in under-exposed regions and to reduce the noise in observations. From experiments it has been noted that the maximum laser intensity of 40% used in practice (due to concerns about the life length of the sensor) is typically too low to utilize the full dynamic range of the sensor. In other words, the dynamic range of this sensor is not the limiting factor in practice, which means that there is no need to increase it. Due to these practical circumstances, an HDR algorithm for the photon counter has not been developed, although it would potentially be useful in a scenario where a higher laser intensity could be utilized.

3.3.2 The PMT sensor

For the PMT the underlying statistical variation which govern the variation observed in the images is more difficult to model in detail than in the case of the photon counting sensor. As stated in section C.2 the stage gain of the PMT does likely not follow the traditionally assumed Poisson distribution but should instead more accurately be modelled by a Polya distribution. The parameters of this Polya distribution would have to be estimated through carefully designed experiments which require a great deal of knowledge about the technical specifications of the PMT. Not only would this process be complicated and time-consuming but it would also require access to information which in the present case is confidential and thus not revealed by the manufacturer of the microscope. Due to the highly impractical nature of this process a decision was made against doing detailed modelling of each individual noise source listed in section 2.1.2. Instead, a simplified approach will be taken where we assume that the total noise contribution to the measured signal can be modelled as independent Gaussian (normal distributed) random variables. This approximation of the total noise is also employed by e.g. [9, 16] when conducting HDR imaging in photography and is often used to model image noise in more general imaging applications.

Recall that since the sensor of the microscope has a limited dynamic range, the observed intensity value will sometimes be saturated. In statistics, this is known as censoring. Censored data means that a value is only partially known, e.g. in the case of observing a pixel value equal to 1, we know that in reality the area has a brightness which corresponds to a pixel value greater than or equal to 1, but due to the limited dynamic range of the sensor we cannot observe the true value. This is an important aspect to keep in mind during the modelling process and a decision has to be made regarding how this behaviour should be implemented into the model.

3.3.2.1 The LS method

An investigation concerning a potential model for the observed intensity as a function of the sensor gain was performed on the dataset *pmt_2* consisting of 25 images with a gain in the range 50-1250 V. Different relations such as low-degree polynomials, a gamma curve ($I(x) = \alpha + \beta \cdot x^{\gamma}$), exponential functions as well as sigmoid functions were tested. Out of these functions, the sigmoid functions seemed to give the best fit in general, although it was difficult to qualitatively evaluate which of the sigmoid functions had the best fit. With $I(x)$ denoting the observed intensity of a given pixel at gain x, the following functions were tested

List 3.1

(1) The error function: $I(x) = \alpha \cdot \text{erf}(\gamma(x - \beta)) + \delta$

(2) The hyperbolic tangent: $I(x) = \alpha \cdot \tanh(\gamma(x - \beta)) + \delta$

(3) The arctangent function: $I(x) = \alpha \cdot \arctan(\gamma(x - \beta)) + \delta$

(4) The Gudermannian function: $I(x) = \alpha \cdot \text{gd}(\gamma(x - \beta)) + \delta$

(5) An algebraic function: $I(x) = \alpha \cdot \frac{\gamma(x-\beta)}{\sqrt{1+(\gamma(x-\beta))^2}} + \delta$

(6) A special case of the logistic function: $I(x) = (1 + \alpha e^{-\gamma(x-\beta)})^{-1} + \delta$

(7) Another algebraic function (the function [11] primarily uses): $I(x) = \left(\frac{e^{\alpha}x^{\gamma}}{e^{\alpha}x^{\gamma}+1}\right)^{\beta}$

(8) The minimum of an exponential function and 1: $I(x) = \min(\alpha \cdot e^{\beta x} + \gamma, 1)$

The parameters were estimated by solving the corresponding non-linear LS problem. Note that the parameters α, β, γ and δ should be estimated independently for each model and each pixel. It should be mentioned that an exponential function, $I(x) = \alpha e^{\beta x} + \gamma$, seemed to be a good fit for pixel values which had no or very few saturated values. This could be interpreted as the exponential model being a good model for the ”true” signal, before it is detected, processed and thereby (potentially) censored due to the limited dynamic range of the sensor. This observation is what motivated the inclusion of function (8) of List 3.1, a function which is not found in the literature (and technically is not a sigmoid).

In order to get more extensive data on which the function of List 3.1 could be tested, another dataset was collected. *pmt_3* contains a series of 1312 images captured at distinct gain levels in the interval $[0, 1250]$. From this dataset it is clear that the saturation occurs rather abruptly and the curve more closely resembles a cut-off exponential function than a smooth sigmoid. As such, function (8) of List 3.1 is not unexpectedly found to be the best fit for the pixels which have several saturated values.

When testing the sigmoid functions for this dataset it also became clear that the deviations from the suggested models seemed to start off small for gains corresponding to poorly exposed pixels, then increase with gain until the pixels started to saturate, at which point the deviations became small again. This observation has two implications. First, since the residual (and thus also the noise) varies with the gain, a regular LS method might not be the best way to estimate the model parameters as it assumes that the noise is constant. Secondly, it implies that the current model fitting seemed to have the poorest performance for intensity values close to the midpoint of the available range. This area should in theory be the region where we have the most confidence in the accuracy of the observations as the limited dynamic range of the sensor is not affecting the observations. It was therefore hypothesized that an ML method might be able to produce a more suitable model which, among other benefits, can handle arbitrary variance models.

3.3.2.2 The ML method

A natural way of improving the results obtained from an LS model fitting is to instead use an ML method of estimating model parameters. Assume that there exists a sample $S = \{x_i : i = 1, 2, .., n\}$ of n observations which are independent and identically distributed. Suppose further that all observations come from a distribution with an unknown probability density function (PDF) $f_0 = f(\cdot \,|\, \theta_0)$ but that the distribution belongs to some known family of distributions $D = \{f(\cdot \,|\, \theta) : \theta \in \Theta\}$, where θ is the vector of parameters for the specific distribution. In order to estimate the unknown θ_0, the estimate $\hat{\theta}$ is desired. We note that the joint density for all observations in S is given by

$$f(S \,|\, \theta) = \prod_{i=1}^{n} f(x_i \,|\, \theta) \tag{3.2}$$

since the observations are independent and identically distributed. The likelihood function L is defined as

$$L(\theta\,;\, S) = f(S \,|\, \theta) = \prod_{i=1}^{n} f(x_i \,|\, \theta) \tag{3.3}$$

which means that the log-likelihood function, the natural logarithm of L, can be written

$$\log(L(\theta\,; S)) = \sum_{i=1}^{n} \log(f(x_i \,|\, \theta)) \tag{3.4}$$

The goal is to find the $\hat{\theta}$ which maximizes $L(\theta; S)$ since this implies that $f(\cdot; \hat{\theta})$ will be the PDF which is the most probable given the observed sample for the assumed family of distributions D. The maximum likelihood estimation (MLE) is thus defined as

$$\{\hat{\theta}\} \subseteq \{\underset{\theta \in \Theta}{\operatorname{argmax}}\, L(\theta\,; S)\} \tag{3.5}$$

given that a maximum exists. Note that maximizing $\log(L(\theta\,; S))$ is equivalent to maximizing $L(\theta; S)$ due to the monotonicity of the logarithm function. Therefore

$\log(L(\theta\,;S))$ is maximized instead of L to find $\hat{\theta}$ in practice, since it is generally easier to find the optimum of a sum than of a product.

Now, consider an arbitrary pixel i of an LDR image and let

$$Y(x,\boldsymbol{\theta}) = h(g(x),\boldsymbol{\theta}) \tag{3.6}$$

where $g(x)$ is the observed intensity of pixel i observed for gain x, $\boldsymbol{\theta}$ is a vector of model parameters specific to pixel i and $h(\cdot,\boldsymbol{\theta})$ is a family of transformations which depend on $\boldsymbol{\theta}$ (leaving out the i subscripts). Furthermore, assume that $Y(x,\boldsymbol{\theta})$ can be modelled through

$$Y(x,\boldsymbol{\theta}) = I(x,\boldsymbol{\theta}) + \varepsilon(x,\boldsymbol{\theta}) \tag{3.7}$$

where $I(x,\boldsymbol{\theta})$ is a mean function and $\varepsilon(x,\boldsymbol{\theta}) \sim N(0,\sigma^2(x,\boldsymbol{\theta}))$. In other words, $Y(x,\boldsymbol{\theta})$ is a normally distributed random variable with mean value $\mathrm{E}[Y(x,\boldsymbol{\theta})] = I(x,\boldsymbol{\theta})$ and variance $\mathrm{Var}[Y(x,\boldsymbol{\theta})] = \sigma^2(x,\boldsymbol{\theta})$.

The fact that $g(x)$ is censored at 1 means that $Y(x,\boldsymbol{\theta})$ is censored as well, but at a different level. Since $g(x) = 1$ is equivalent to $Y(x,\boldsymbol{\theta}) = h(1,\boldsymbol{\theta}) \coloneqq l$ we have that the censoring level for $Y(x,\boldsymbol{\theta})$ is given by l.

The aim is to fit the model given by eq (3.7) to data and thereby obtain an estimate of the uncensored intensity. To this end, consider an image series S consisting of n LDR images which differ only by the gain x_j, $j = 1,2,..,n$, used to capture the images. Let P be the set of pixels which are studied and let $A = \{x : x \in \{x_j\}_{j=1}^n\}$ be the set of observations for pixel i which will be used to estimate the coefficients of the model.

The likelihood function for this problem takes on a special form due to the censoring of data which occurs for high intensity values. To account for the censored data we adopt a likelihood method similar to that used in [17] (see in particular equation (12)). Let $A_1 = \{x \in A : Y(x,\boldsymbol{\theta}) < l\}$ and $A_2 = \{x \in A : Y(x,\boldsymbol{\theta}) \geq l\}$ be the sets of observations which are uncensored and censored, respectively. The log-likelihood function is then given by

$$L = L_1 + L_2 \tag{3.8}$$

where

$$L_1 = \sum_{x\in A_1} \log\left[f_Y(Y(x,\boldsymbol{\theta}))\right] = \sum_{x\in A_1} \log\left[\frac{1}{\sigma(x,\boldsymbol{\theta})}\phi\Big(\frac{Y(x,\boldsymbol{\theta}) - I(x,\boldsymbol{\theta})}{\sigma(x,\boldsymbol{\theta})}\Big)\right] \tag{3.9}$$

and

$$\begin{aligned} L_2 &= \sum_{x \in A_2} \log \left[P(Y(x, \boldsymbol{\theta}) \geq l) \right] = \sum_{x \in A_2} \log \left[1 - P(Y(x, \boldsymbol{\theta}) \leq l) \right] = \\ &= \sum_{x \in A_2} \log \left[1 - F_{Y(x,\theta)}(l) \right] = \sum_{x \in A_2} \log \left[1 - \Phi\Big(\frac{l - I(x, \boldsymbol{\theta})}{\sigma(x, \boldsymbol{\theta})} \Big) \right] \end{aligned} \tag{3.10}$$

where $f_Y(\cdot)$ and $F_Y(\cdot)$ are the PDF and cumulative distribution function (CDF) of $Y(x, \boldsymbol{\theta})$ respectively and $\phi(\cdot)$ and $\Phi(\cdot)$ are the standardized normal PDF and CDF respectively. The expression in eq (3.8) should be maximized in order to find the ML estimate $\hat{\boldsymbol{\theta}}$. Note that this is a constrained optimization problem as we require that $I(x, \boldsymbol{\theta})$ is an increasing function and $\sigma^2(x, \boldsymbol{\theta}) > 0$. Note also that since $\boldsymbol{\theta}$ is pixel dependent, the MLE is performed independently for each pixel.

Possible choices of transforms $h(\cdot, \boldsymbol{\theta})$ of the observed pixel intensities $g(x)$ are the identity transform,

$$Y(x, \boldsymbol{\theta}) = g(x), \tag{3.11}$$

or the shifted logarithmic transform,

$$Y(x, \boldsymbol{\theta}) = \log \left(g(x) - \lambda \right), \tag{3.12}$$

or the Box-Cox transformation,

$$Y(x, \boldsymbol{\theta}) = g(x)'(\lambda), \tag{3.13}$$

where the prime $(\cdot)'(\lambda)$ denotes the Box-Cox transformation

$$x'(\delta) = \begin{cases} \frac{x^\delta - 1}{\delta} & \text{if } \delta \neq 0 \\ \log(x) & \text{if } \delta = 0 \end{cases}. \tag{3.14}$$

A list of possible mean functions $I(x, \boldsymbol{\theta})$ is given in List 3.2 and a list of possible variance functions $\sigma^2(x, \boldsymbol{\theta})$ is given in List 3.3.

List 3.2

(1) $I(x, \boldsymbol{\theta}) = \alpha e^{\beta(x'(\delta) - x_0)} + \gamma$

(2) $I(x, \boldsymbol{\theta}) = \alpha e^{\beta x^2 + \varphi x + x_0} + \gamma$

(3) $I(x, \boldsymbol{\theta}) = \alpha e^{\beta x} + \gamma$

List 3.3

(1) $\sigma^2(x, \boldsymbol{\theta}) = c$

(2) $\sigma^2(x, \boldsymbol{\theta}) = ax^b + c$

(3) $\sigma^2(x, \boldsymbol{\theta}) = ax^2 + bx + c$

(4) $\sigma^2(x, \boldsymbol{\theta}) = ae^{bx}$

(5) $\sigma^2(x, \boldsymbol{\theta}) = ae^{bx} + c$

(6) $\sigma^2(x, \boldsymbol{\theta}) = ae^{b(x-d)} + c$

(7) $\sigma^2(x, \boldsymbol{\theta}) = ae^{bx'(\delta)} + c$ (same δ as for the mean function if applicable)

(8) $\sigma^2(x, \boldsymbol{\theta}) = ae^{bx'(\delta_2)} + c$ ($\delta_2 \neq \delta$ with δ from the mean function if applicable)

(9) $\sigma^2(x, \boldsymbol{\theta}) = ae^{p_2x^2+p_1x+p_0} + c$

With the 3 different possible transformations given by equations (3.12), (3.14) and (3.11) as well as the different functions in Lists 3.2 and 3.3 this makes for a total of 75 distinct combinations (for mean functions (2) and (3) variance functions (7) and (8) are the same). A majority of these combinations have been tested on data by means of solving the corresponding ML optimization problem and comparing the model response to observed data. Those combinations which have not been tested have been ruled out based on previously obtained results. For example, if a given data transformation h and mean function I gave virtually the same results (in terms of quality) using variance function (4) and variance function (6) there is no need to test variance function (5) as (6) contains (5) as a special case ($d = 0$).

When judging the quality of the different models they were assessed based on three different criteria. The most important criteria is how accurately the model agree with observed data, known as the model fit or the accuracy of the model. Having an accurate model predicting the intensity response as a function of gain is the single most important piece of the puzzle when constructing an HDR image. The second most important criteria is the number of model parameters which are necessary to estimate. If too many parameters are used there is a risk of model overfitting which makes the model unreliable in areas where there is no data available, e.g. between obtained data points or for points which lie outside the observable set of points. As such, if there are two models that have negligible differences in accuracy and require different number of parameters the model with the fewest parameters will be preferred over the model with additional parameters. This is the reason as to why lists 3.2 and 3.3 not only include the most general forms of each model. The third criteria is the computational performance of the model, i.e. how much cpu time is needed to solve the model. Although having a computationally fast model is certainly preferable, it is in this particular case proposed that speed improvement should not come at the cost of model accuracy.

In order to improve the quality of the model with respect to the second criteria, that the number of model parameters estimated for each pixel should be as few as possible, a parameter reduction procedure was carried out. For this procedure, the model

$$\begin{aligned} I(x,i) &= \alpha e^{\beta(x'(\delta)-x_0)} + \gamma \\ \sigma^2(x,i) &= a e^{bx} \end{aligned} \tag{3.15}$$

for identity transformed data (eq. (3.11)) was chosen as the foundation model. This choice was made based on the fact that the model proved to provide very accurate fits but also had some pairs of model parameters which turned out to be strongly correlated. Therefore, for one parameter at a time, it was tested whether or not a given parameter could be omitted completely (i.e. be set to 0 or 1 depending on the parameter in question) or if it was possible to find a different constant parameter value which could be set prior to the estimation of the other parameters and thereby be used for all pixels whilst still resulting in an accurate model. In the case of estimating a constant parameter value, this estimate was obtained by letting the parameter be fitted independently for each pixel along with the other parameters and then choosing the fixed parameter value to be either the mean or the median (depending on how large the variations were) of these estimates. This parameter reduction procedure resulted in the model

$$\begin{aligned} I(x,i) &= \alpha_i e^{\beta_i(x'(\delta)-x_0)} \\ \sigma^2(x,i) &= a_i e^{bx} \end{aligned} \tag{3.16}$$

where only the 3 parameters α_i, β_i and a_i need to be fitted individually for each pixel (denoted by the subscript i), the parameters δ, x_0 and b are pixel-independent parameters and γ in eq. (3.15) is removed (set to 0). This model is faster to solve and does not have strongly correlated parameters whilst providing fits indistinguishable in terms of accuracy from those produced by the model given by eq. (3.15). It should be noted that although the values of δ, x_0 and b are fitted from data coming from a single sample, these values have subsequently been used for several other samples and has provided accurate fits in all cases. As such, it is sufficient to determine δ, x_0 and b once and then use the same obtained values in all subsequent estimations.

Once a model has been fitted it will be used to estimate the true (non-noisy and non-censored) response of the camera sensor for a given pixel. For pixels which do not saturate and thus are not censored the main benefit of the HDR composition will be noise reduction. This noise reduction is achieved by interpolating the fitted model within the range of observed values. For pixels which do saturate the main benefit of the HDR composition is the ”un-censoring” of data. This un-censoring is achieved by using the fitted model to extrapolate to intensities greater than 1, i.e. outside the range of observable values. With regard to extrapolation one should be very careful with how far from the observable data the extrapolation is carried out.

Clearly, we do not know what happens outside of the observable range of intensities. It is a sound assumption that the behaviour of the observed data is continued after the point where we can no longer observe it, and for a reasonable model this should be the case for a relatively long range outside the observable range. However, it is still good practice to be reasonably conservative when doing model extrapolation as there are no means of experimentally validating the results.

From the histograms of individual pixels from the dataset *pmt_1* (250 images, constant gain) it seems that the normal distribution of pixel intensities might be a reasonable choice. For the data in *pmt_4* (2500 images, constant gain) the normal distribution provides a good model for the data. This conclusion is reached by comparing the histograms of individual pixel intensities throughout the image series and comparing the shape of the histograms to the shape of the PDF of the normal distribution when the parameters of the distribution are estimated using MLE. This is especially the case for pixels whose mean intensity isn't close to either censoring point (intensity values 0 and 1) which indicates that the normality assumption applies for data which isn't censored. For pixels which have censored observations the ML estimation will fit a truncated normal distribution. We can neither confirm nor deny the normality assumption for these pixels based on the observed data since the true data is not observable.

4

Results

4.1 Photon counter

The dataset *pc_1* was analyzed in order to investigate the assumption that the intensities registered by the photon counter sensor are Poisson distributed. To this end, we consider all pixels for which the mean intensities are greater than E_{lim}. For these pixels, the ratio R given by eq. (C.3) is calculated after which statistics such as the min/max and mean values (of the set of all pixels having sample mean greater than E_{lim}). The results of these calculations are found in table (4.1). Note that increasing E_{lim} means that the pixels have to be increasingly bright (on average) in order to be considered.

From the data provided in the table it seems that $R = 1$ is a very reasonable approximation, in particular for the higher (average) intensity values. For $E_{lim} = 0$ the maximum value 71.0 is clearly much larger than what you would expect if the intensity is indeed Poisson distributed. These outliers are due to the fact that there exist pixels whose intensity is very low (0 or 1 where the whole range is $[0, 2^b - 1]$ where b is the bit depth) for all images but one where the registered intensity is high (50-80). These pixels will have low sample averages, but large variance due to a single large value, leading to a large value of R. The large intensity observed only once in the whole series of 250 images is likely due to a very slight temporary shift in either the sample or some part of the microscope. This kind of observations are extremely rare when looking at the data as a whole, suggesting that their occurrence do not contradict the $R = 1$ hypothesis. It should also be noted that pixels with low average intensity are difficult to analyze due to their nature as the low intensities

E_{lim}	min	max	mean	median	nbr of pixels
0	0.65	71.0	1.01	0.98	1045691
1	0.65	22.9	1.01	1.00	163280
5	0.66	9.79	1.00	0.99	15013
10	0.66	1.58	1.00	1.00	448

Table 4.1: Statistics obtained for the ratio R given by eq. (C.3) for the dataset *pc_1*. For each calculation only pixels having sample mean greater than E_{lim} were considered.

indicate that very little data is available, hence the estimator $\hat{R}$ has a higher variance. As such, the very dark pixels generating samples which do not seem to be Poisson distributed do not necessarily contradict the Poisson hypothesis either, and these pixels should rather be treated as samples for which it is not possible to confirm nor deny the hypothesis.

As E_{lim} is increased, more and more of these outliers are filtered out, as can be seen in table (4.1) by looking at the max value, which decreases. It should be noted that for all values of E_{lim}, tested at least 95% of the considered pixels have R values which lie in the interval $[0.8, 1.2]$ which indicate that the $R = 1$ assumption seems very reasonable for the vast majority of pixels. This in turn speaks in favor of the Poisson distribution.

The model $I_i = \alpha_i \cdot L^{\gamma_i}$ (eq. (3.1)) was proposed in section (3.3.1) as the relationship between the observed image intensity and the laser power used to illuminate the sample. Graphical representation of the results of the curve fitting for the images of dataset *pc_2* can be found in figures (4.1) and (4.2). The model fits the data quite well for pixels which have a relatively high average intensity. For darker pixels (lower average intensity) the intensity does not necessarily show the same increasing behaviour as that in Figures (4.1) and (4.2). Instead, these pixels have intensities whose variation more resemble those observed when studying dataset *pc_2*, i.e. the laser intensity is constant and the variations are well described by a Poisson process with constant λ. As such, some of these darker pixels would need to be observed under greater illumination (higher laser intensity) in order to obtain sufficiently detailed measurements to do the curve fitting. For other pixels which actually are very dark (i.e. there is nothing but air there to measure) the observed intensity variations will be due to noise for which the modelled gamma curve will not be appropriate.

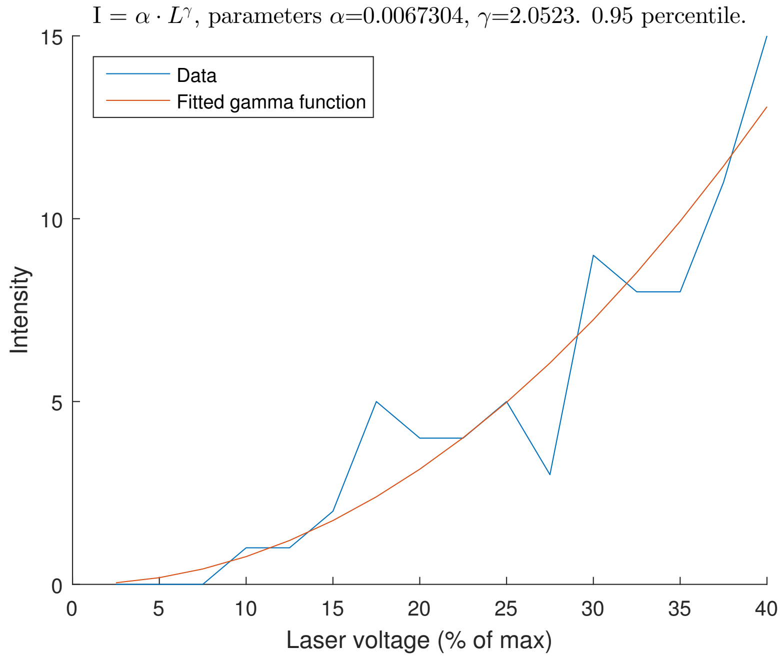

Figure 4.1: Data compared to the fitted function $I = \alpha \cdot L^\gamma$ for a pixel with average intensity greater than 95% of the pixels in the dataset *pc_2*.

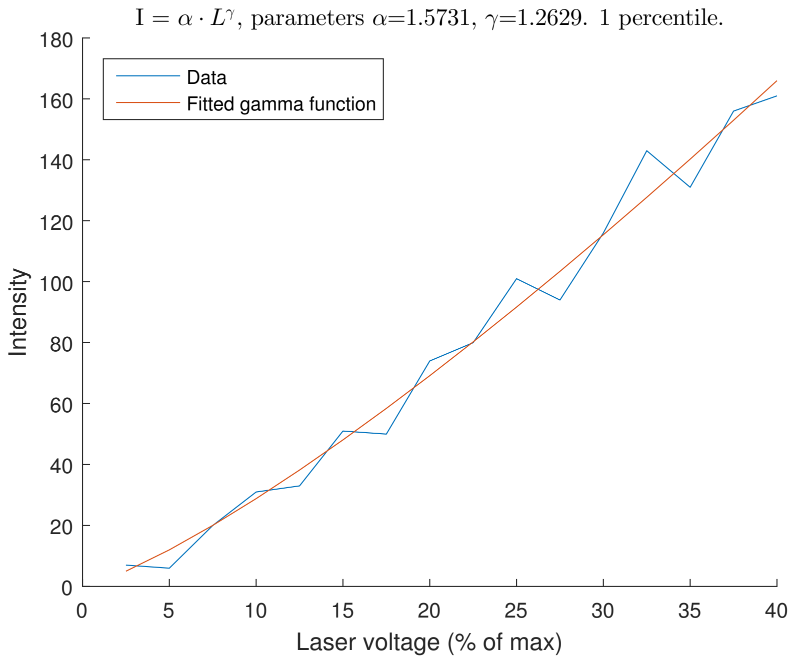

Figure 4.2: Data compared to the fitted function $I = \alpha \cdot L^\gamma$ for the pixel with highest average intensity in the dataset *pc_2*.

4.2 PMT

The LS and the ML methods of estimating the signal outlined in sections 3.3.2.1 and 3.3.2.2, respectively, have been tested for several datasets. As there is no quantitative measure which can be used to evaluate the accuracy of the results they will instead be evaluated based on a visual inspection of plots and generated images. In some cases the images will be presented using another colormap than the traditional grayscale colormap in order to better visualize the results, in particular in the dark regions (low pixel intensity). Whenever this is done, a colorbar relating the displayed colors to numerical values will be shown along with the image. Note that changing the color map is purely a visual aid - the intensity values are not changed by this operation, only the color, to which a certain value is mapped.

The assumption that the images remain static throughout the image capturing process has been investigated by visually inspecting cropped images. For each of the datasets that the HDR algorithm has been applied to (presented in the following sections) there exists a corresponding calibration dataset. This calibration dataset was captured directly after the capturing of the primary dataset and was conducted in exactly the same manner as when capturing the primary dataset except that the gain was kept constant. Thus, this calibration dataset can be used to investigate movement between images since the number of images captured and the total time of capturing the images is the same as for the primary dataset. Based on this investigation it seems that the assumption of static samples is valid as no signs of movements could be detected, neither between the first image and the last image of a dataset nor between consecutive images. Examples of some of the figures evaluated during this calibration process can be found in section B.3.

4.2.1 Results of the LS modelling

Results for individual pixels when applying the LS model on the images in dataset *pmt_3* can be found in Figure 4.3. As is seen in the figure the function $I(x) = min(\alpha e^{\beta x} + \gamma, 1)$ provides a reasonable model for how the observed pixel intensity varies with gain. It is therefore possible to generate images which simulate any specific gain by first fitting the parameters α, β and γ for each individual pixel and then evaluate $I(x)$ for the desired gain level, yielding the predicted pixel intensity. An image generated in this manner will have reduced noise compared to the original LDR images, since raw data from several images are used to fit the parameters. Thus, this process is conceptually similar to frame averaging. Comparisons between the original image and a generated image simulating the same gain can be found in Figures 4.4 and 4.7 for two different gain levels. These figures show that the generated image does indeed have reduced noise, giving it a smoother appearance. The effect of the noise reduction can be clarified further from Figure 4.6 where the variation of intensity as a function of gain is plotted for the pixels which have the largest differences between original and generated image. For the specified gain (699.2 V) these pixels have an observed intensity which is very different from the intensity observed for slightly smaller and larger gains, indicating that the observation for this particular gain is very noisy. The intensity predicted by $I(x)$ (marked in the figure with a blue star) is much more likely than the observed intensity to be an accurate prediction of the true intensity.

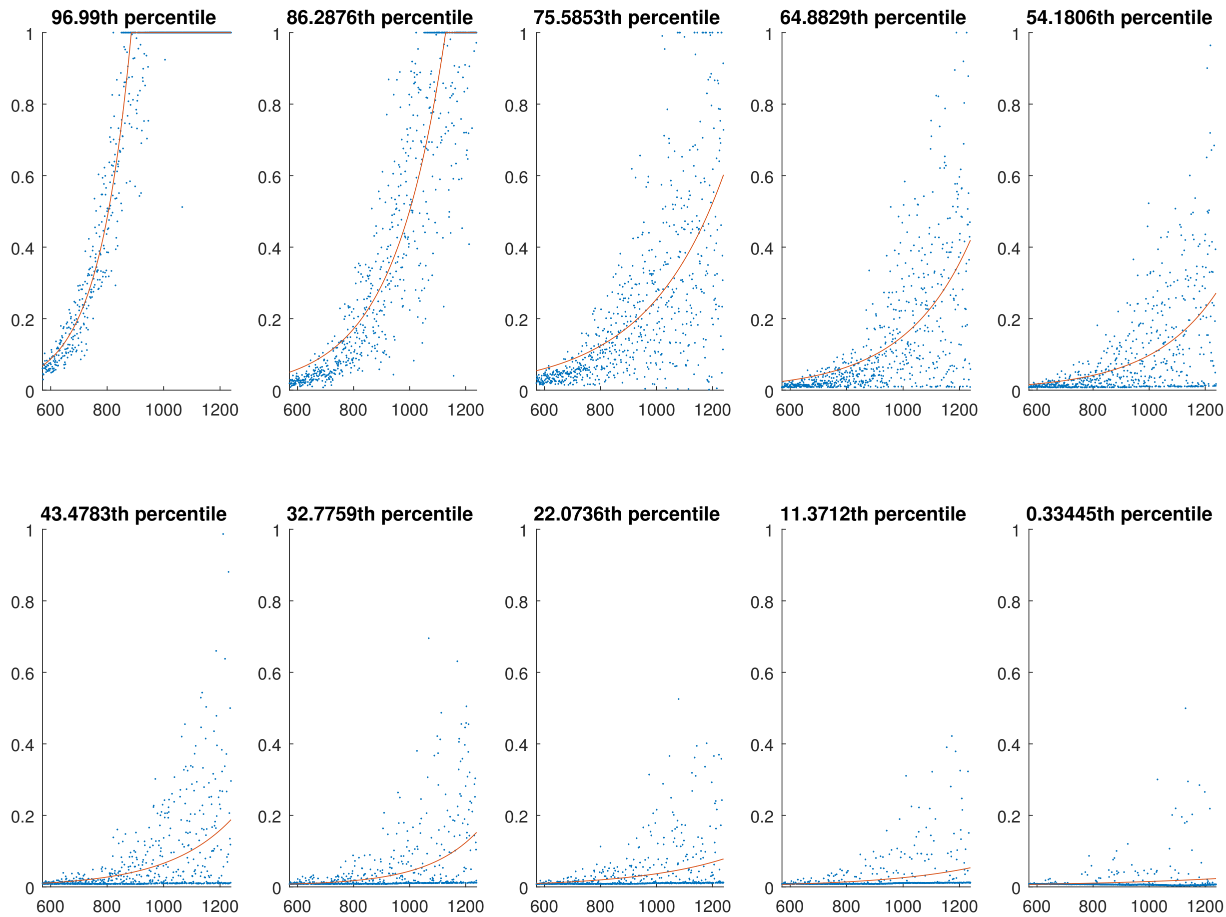

Figure 4.3: Results of modelling the observed pixel intensity (blue) by the model $I(x) = \min(\alpha e^{\beta x} + \gamma, 1)$ (red) where x is the gain for a few different percentiles of average pixel intensity. The model parameters are estimated individually for each pixel using LS. The model has been applied to the dataset *pmt_3_trunc*.

From Figure 4.3 it is also clear that the model leaves room for improvement. For percentiles 86.2876, 75.5853 and 64.8829 the first parts (approximately gain $x \in [571.13, 800]$) of the fitted functions are not as good as for other percentiles. This means that for these pixels the predicted pixel intensity might be slightly inaccurate if an image were to be simulated for $x \in [571.13, 800]$). One way of working around this would be to simulate an image for a gain slightly higher than 800, where the fit is more accurate. This should however be done with care, as the brightest pixels of this dataset (percentile greater than 96.99) might have saturated before gain 800, meaning that for these pixels an evaluation at gain greater than 800 might require a rather long extrapolation. A detailed examination of the dataset shows that it is only the very brightest pixel of the dataset which clearly saturates before gain 800. This implies that in this case there is only one pixel in the whole dataset for which the extrapolation is very long, meaning that we are putting a lot of stress on the regression model, and the validity of the model at this range is in question for this particular pixel.

From Figures (4.5) and (4.8), which show the absolute difference between the original image and the generated image, two interesting observations can be made. First, the main features of the structure which can be seen in the original and generated images are also visible in the difference between the two images. Hence, where the largest differences occur is where there is a structure to be observed which in turn implies that the greatest benefit obtained from the noise reduction is more accurate information about the material itself. Second, the differences between the generated image and the original seem to be increasing with gain. This is in line with expectations since the variation in pixel intensities (and thus the noise) for a fixed pixel increases with gain as can be seen by carefully studying the graphs where pixel intensity is plotted as a function of gain (Figures (4.3) and (4.6)).

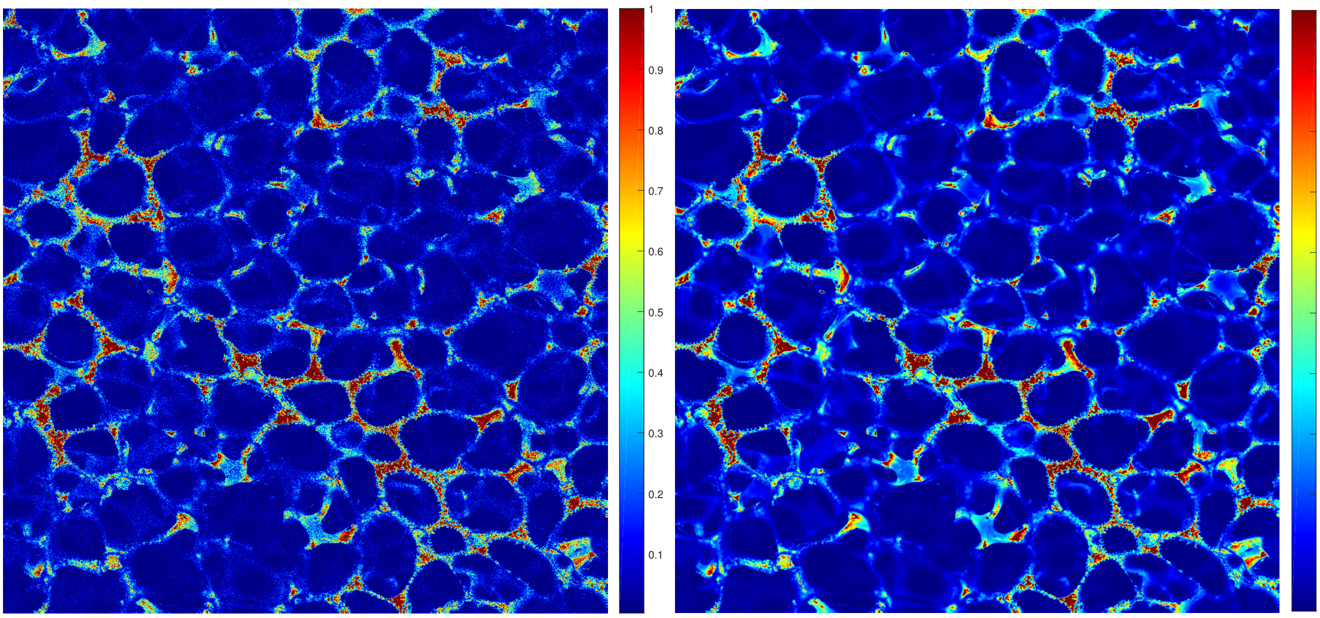

Figure 4.4: The actual image captured at gain 850.5 V (left). The generated (computer simulated) image for gain 850.5 V (right). The function $I(x) = min(\alpha e^{\beta x} + \gamma, 1)$ was fitted individually for each pixel and the generated pixel value was obtained by evaluating $I(x)$ at the specific gain level. The images are taken from dataset *pmt_3_trunc*.

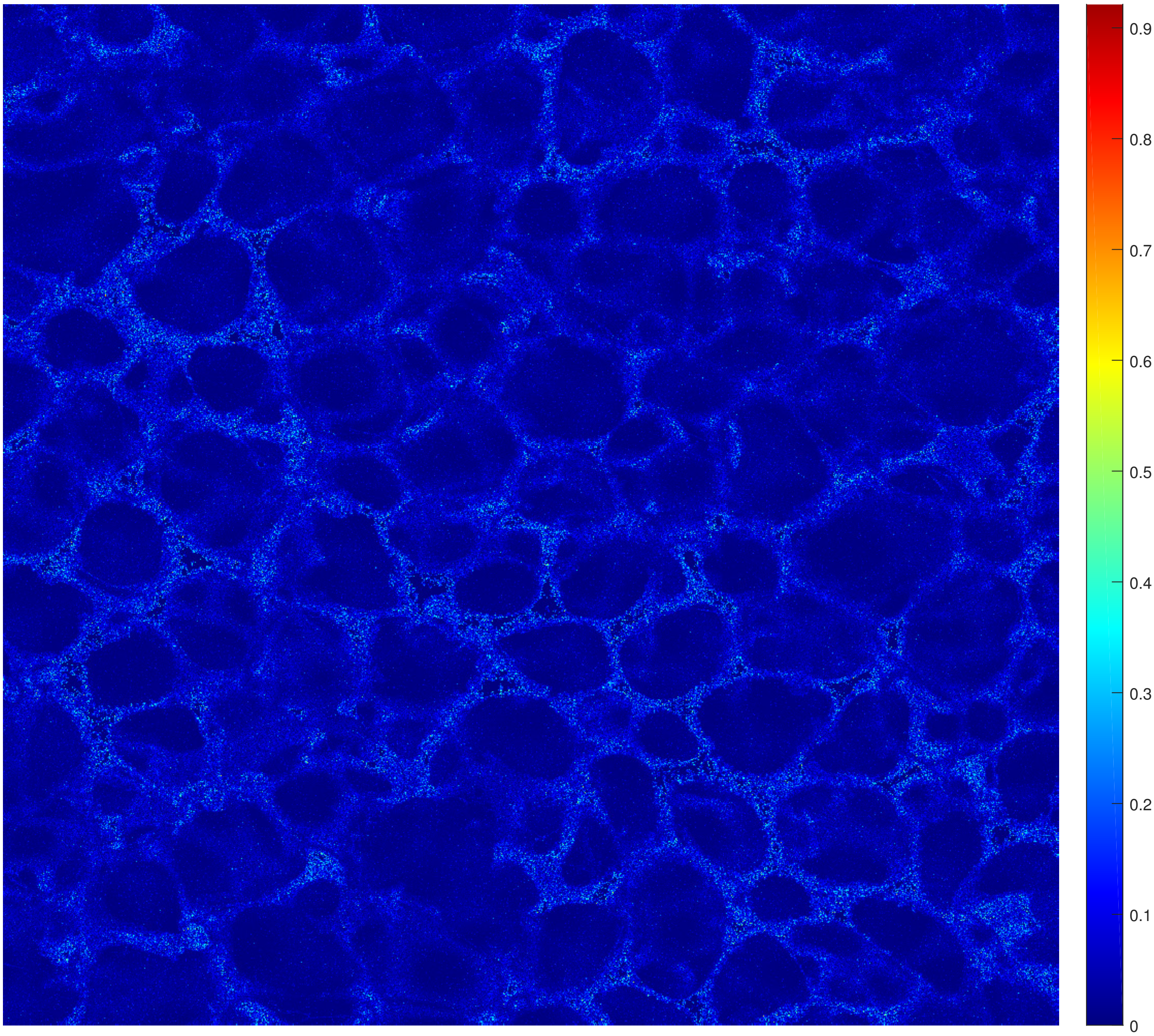

Figure 4.5: The absolute difference between the two images in Figure 4.4.

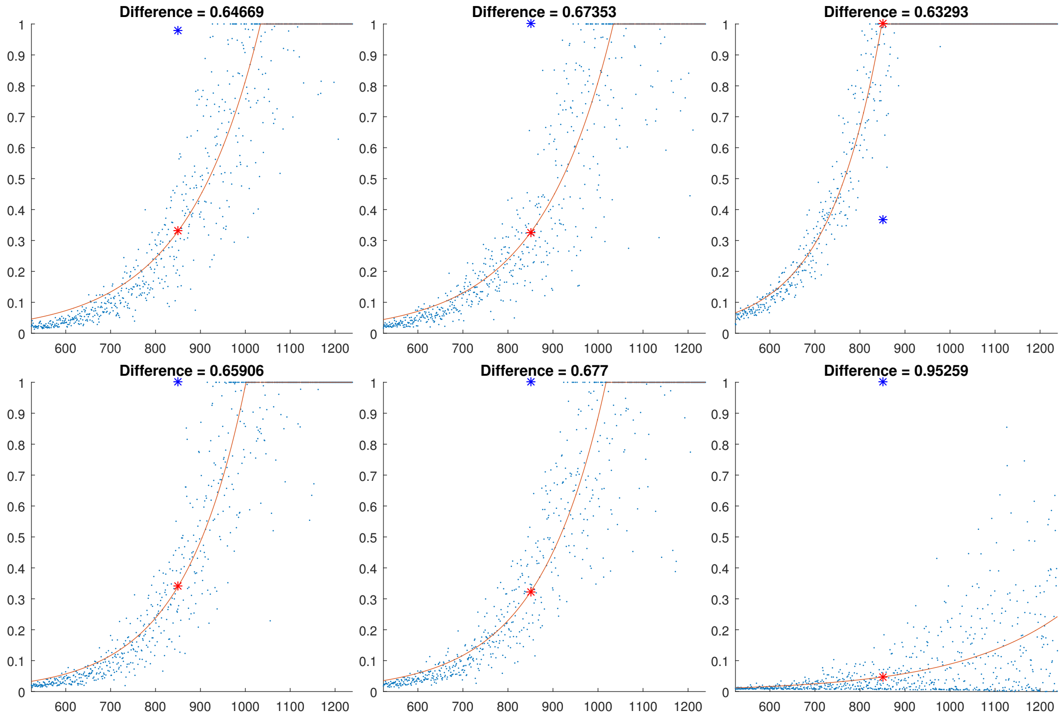

Figure 4.6: Plots of the observed pixel intensity (y-axis) as a function of gain (x-axis) for the observed data (blue dots) and the fitted function (red line). The pixels shown here are the pixels which in Figure 4.5 have a high intensity, i.e. pixels for which large differences are observed between the reference image and the generated image. By using the interpolated value (red star) instead of the observed value (blue star), a noise reduction is achieved.

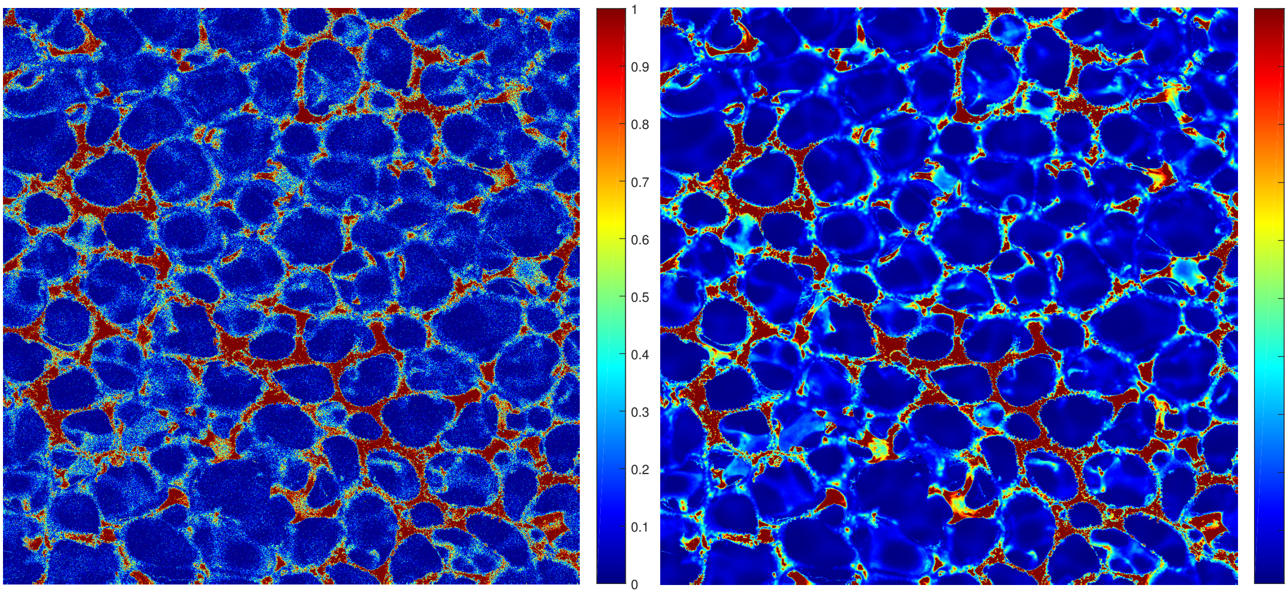

Figure 4.7: The actual image captured at gain 1000.2 V (left). The generated (computer simulated) image for gain 1000.2 V (right). The function $I(x) = min(\alpha e^{\beta x} + \gamma, 1)$ was fitted individually for each pixel and the generated pixel value is obtained by evaluating $I(x)$ at the specific gain level. The images are taken from dataset *pmt_3_trunc*.

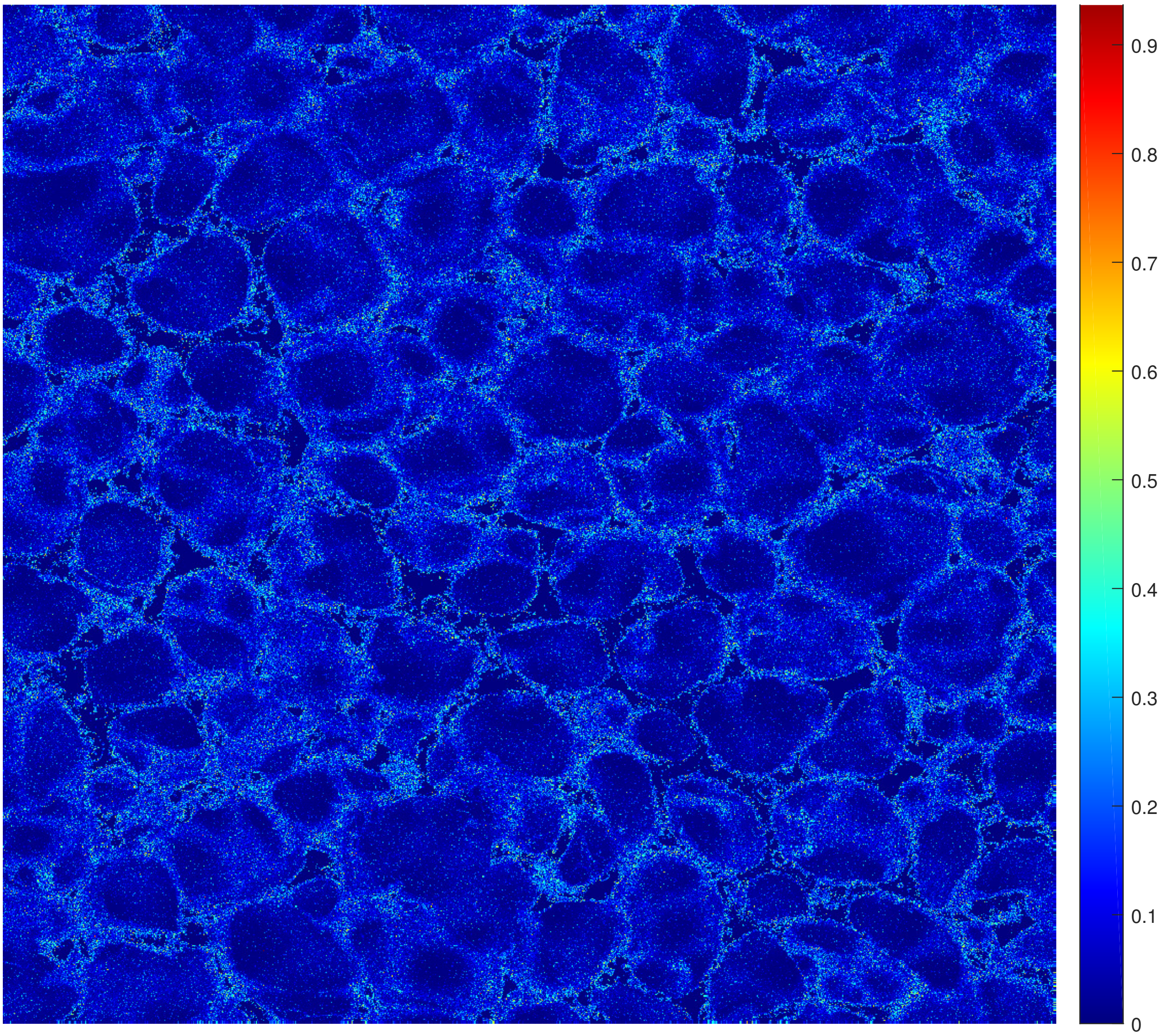

Figure 4.8: The absolute difference between images in Figure 4.7. Differences are in general much larger for this gain (1000.2 V) than for a lower gain of 850.5 (Figure 4.5), except for the (on average) brightest pixels which saturate in both cases and thus have a difference equal to 0.

From Figures (4.9)-(4.11) it is clear that the applied LS model has produced an image with less noise and simulates a camera sensor with satisfactory dynamic range to capture the whole range of intensities necessary. In the zoom-ins we see that small and very thin thread-like details are now visible which could not be seen in the original image. Some areas which appear completely dark in the original image now shows structures which appear to be part of the material which lie on a different z-level than the confocal plane, i.e. on a different physical depth.

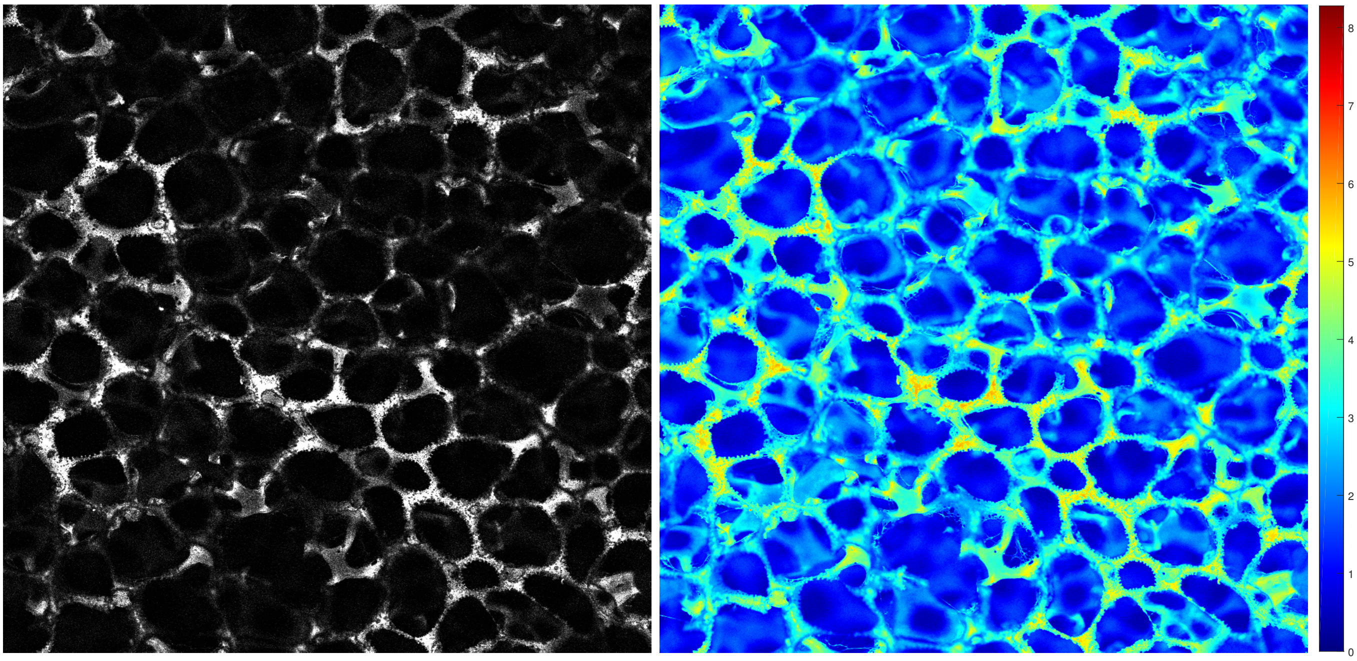

Figure 4.9: The original image captured with the microscope at gain 850.5 V (left). This image has approximately $6 \cdot 10^4$ saturated pixels. The generated (computer simulated) image for the same gain (right). The function $I(x) = min(\alpha e^{\beta x} + \gamma, 1)$ was fitted individually for each pixel (using the whole image series as data) and the generated pixel value was obtained by evaluating $\alpha e^{\beta x} + \gamma$ (i.e. $I(x)$ without the minimum operator) at the specific gain level. The image was tone mapped using a logarithmic operator and subsequently shifted such that the lowest recorded intensity is 0. This image has no saturated values. The images are taken from dataset *pmt_3_trunc*.

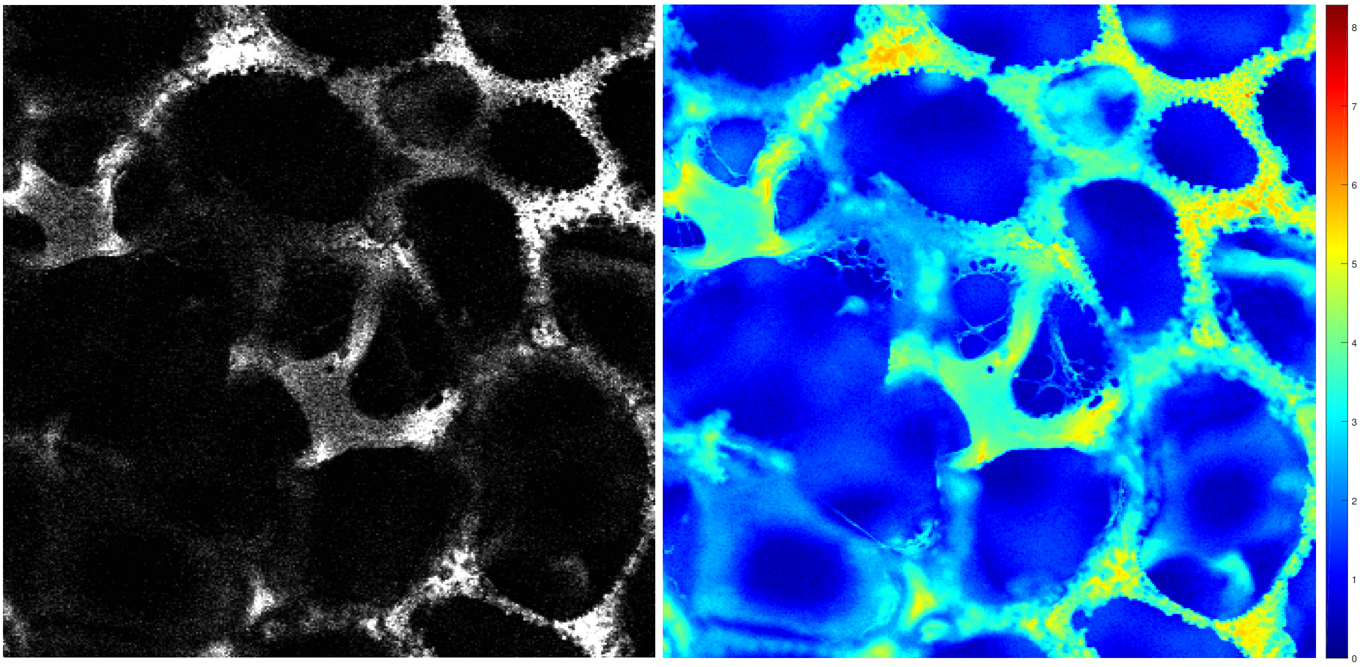

Figure 4.10: Zoom-in of an area of Figure 4.9, both subfigures display the same area.

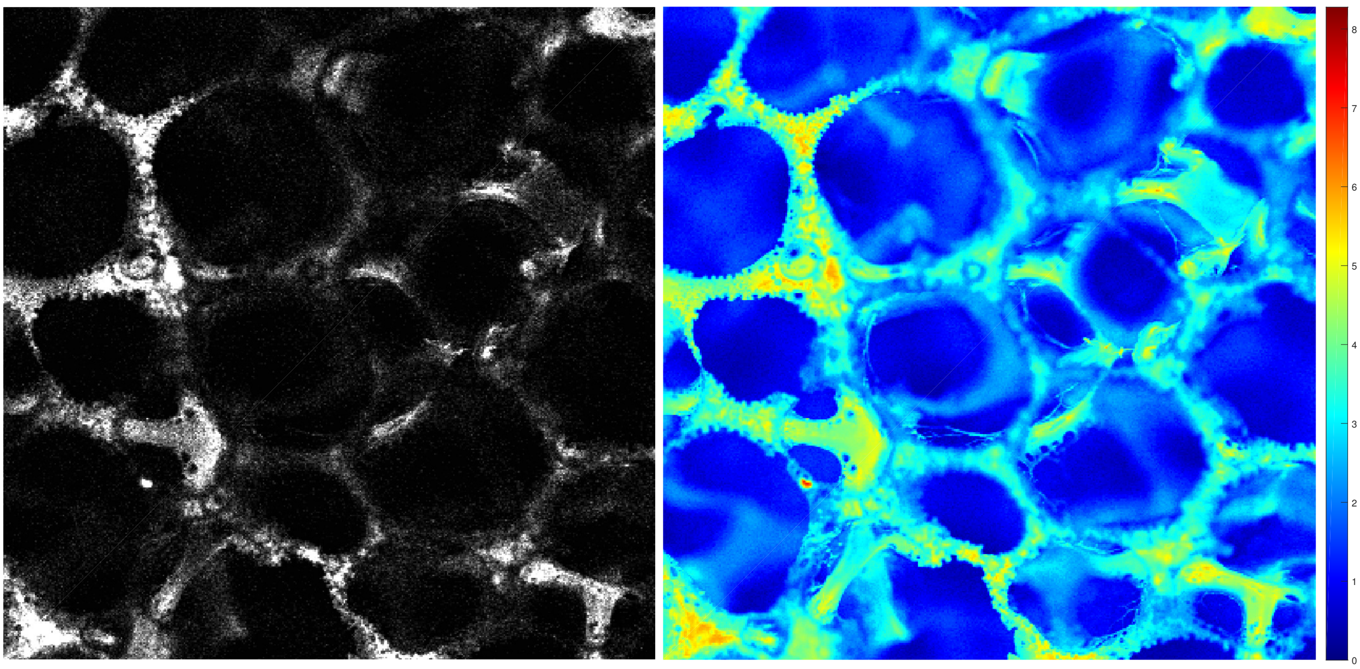

Figure 4.11: Zoom-in of an area of Figure 4.9, both subfigures display the same area.

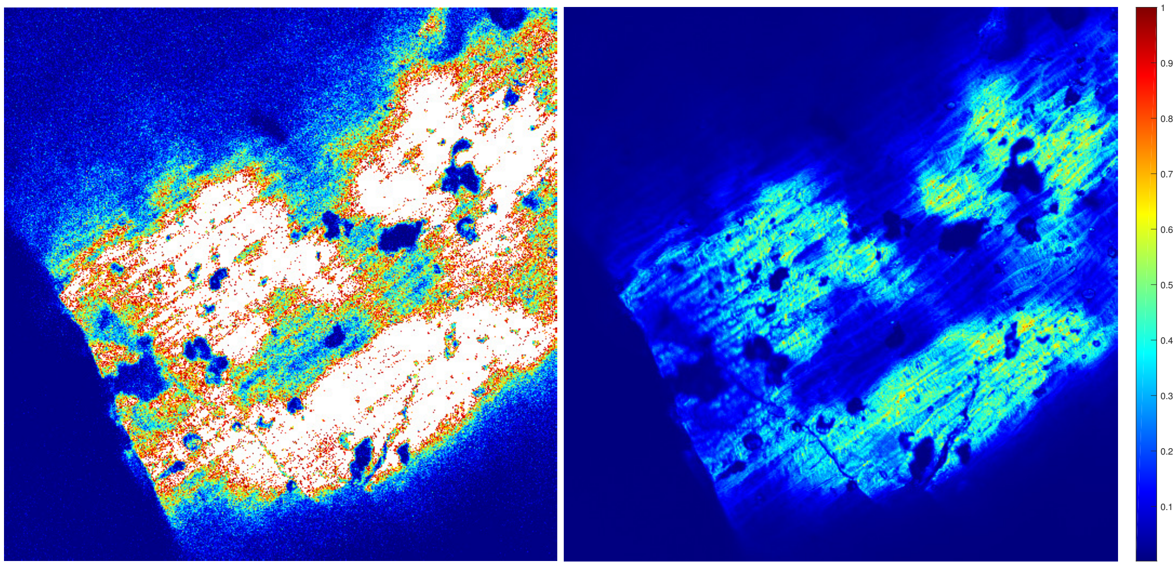

Figure 4.12: The original image captured with the microscope at gain 752 V (left). The generated (computer simulated) image for the same gain (right), obtained through the LS method. Both images use the same color axis where 1 represents the largest intensity (marked with white color) but are normalized by the largest value in each respective image. Images are taken from dataset *wheat_bran*.

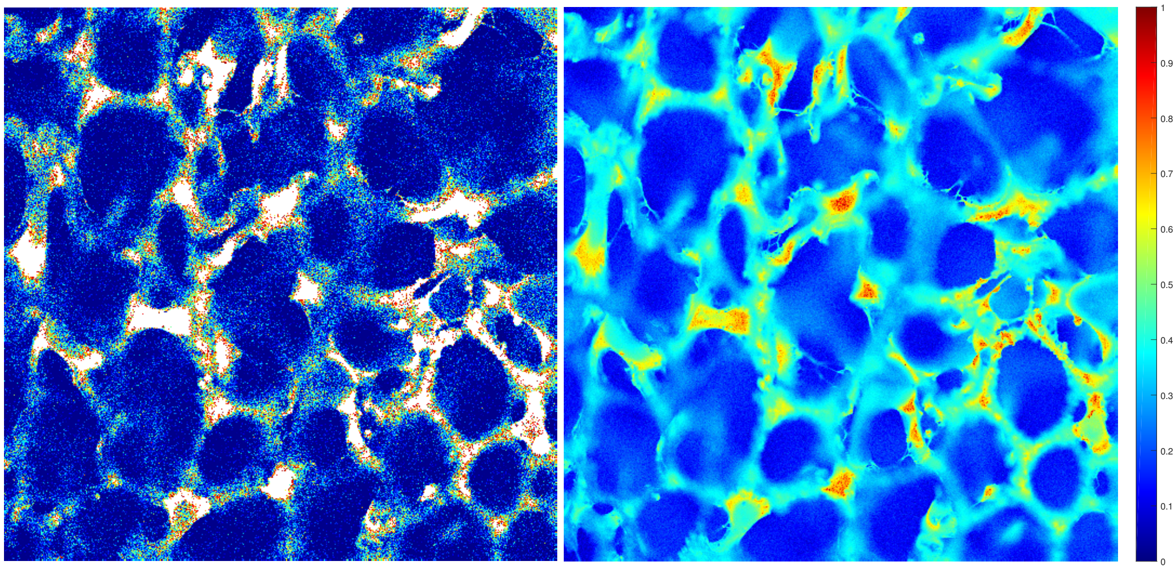

Figure 4.13: The original image captured with the microscope at gain 952 V (left). The generated (computer simulated) image for the same gain (right), obtained through the LS method. The generated image was tone mapped using a logarithmic operator and subsequently shifted such that the lowest recorded intensity is 0. Both images use the same color axis where 1 represents the largest intensity (marked with white color) but are normalized by the largest value in each respective image. Images are taken from dataset *foam*.

Figure 4.14 shows that the censoring is removed using the proposed LS method. Whereas the original intensities were limited to the interval $[0, 1]$, the generated image has pseudo-intensities with unlimited range and as such recreates information which is lost in the LDR images due to the censoring.

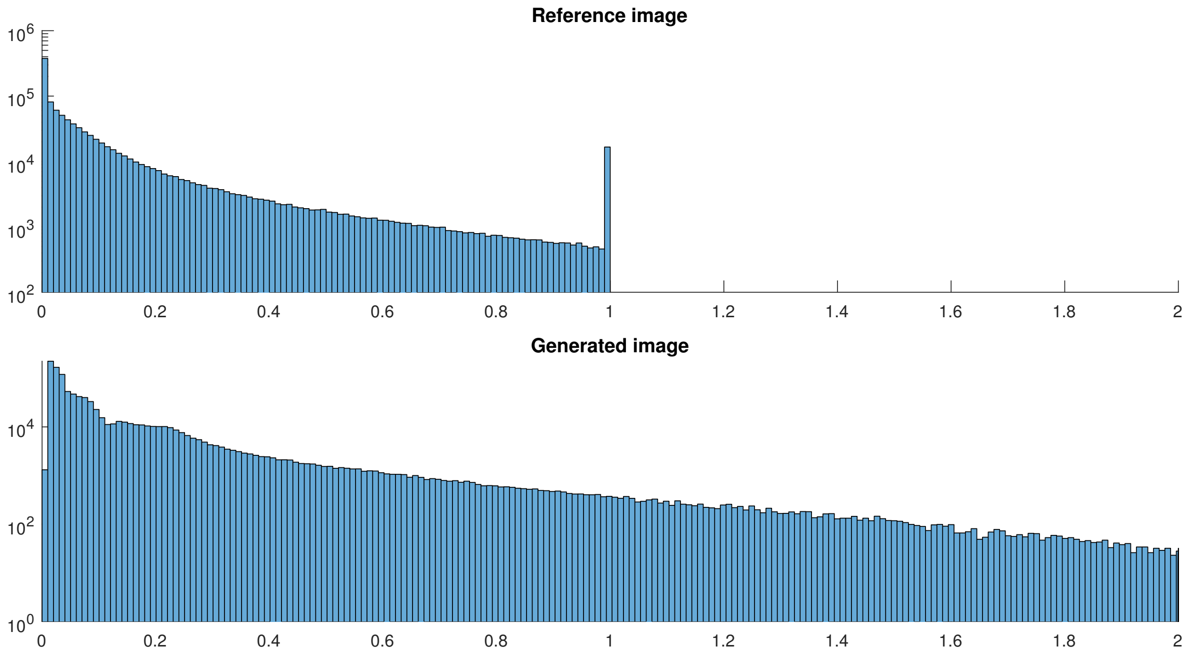

Figure 4.14: Histogram of the pixel intensities of the reference image, i.e. left image in Figure 4.9 (upper). Truncated histogram of the pixel intensities of the generated image, i.e. right image in Figure 4.9 (lower). Note that the y-axis has a logarithmic scale which differs between the two subfigures.

4.2.2 Results of the ML modelling

4.2.2.1 The 7 parameter model

Comparing Figure 4.15 to Figure 4.3 we can in particular note that for percentiles 86.2876, 75.5853 and 64.8829 the first parts (approximately gain $x \in [571.13, 800]$) of the results obtained through the ML method clearly fit the data better than the results obtained using the LS method. For gains larger than 800, the differences in numerical values are generally quite small. However, the fact that the ML results seems to be the best fit overall indicates that for large gains the ML results are to be preferred over the LS results even though their numerical values are very similar. In other words, the results of Figures 4.15 and 4.3 show that the ML method provides a fit which is always better than or on par with the fit provided by the LS method. For the observed data the variation of pixel intensity does not seem to be constant with gain, which the LS method assumes, meaning that the ML method provides a model which better fits data. The ML method also provides a more natural way of modelling the limited dynamic range of the sensor through the use of the likelihood function L_2, equation (3.10), in comparison to the LS method where this behaviour was modelled through the use of the minimum operator.

From Figure 4.16 which compares the results of the LS method to those of the ML method, we note that the overall appearance of the images are quite similar. The ML method generates a larger range of numerical values for the pixel intensities and in order to make the images comparable they are both color scaled using this larger range of values. From Figures (4.15) and (4.16) we can note that the images are similar also on a smaller scale.

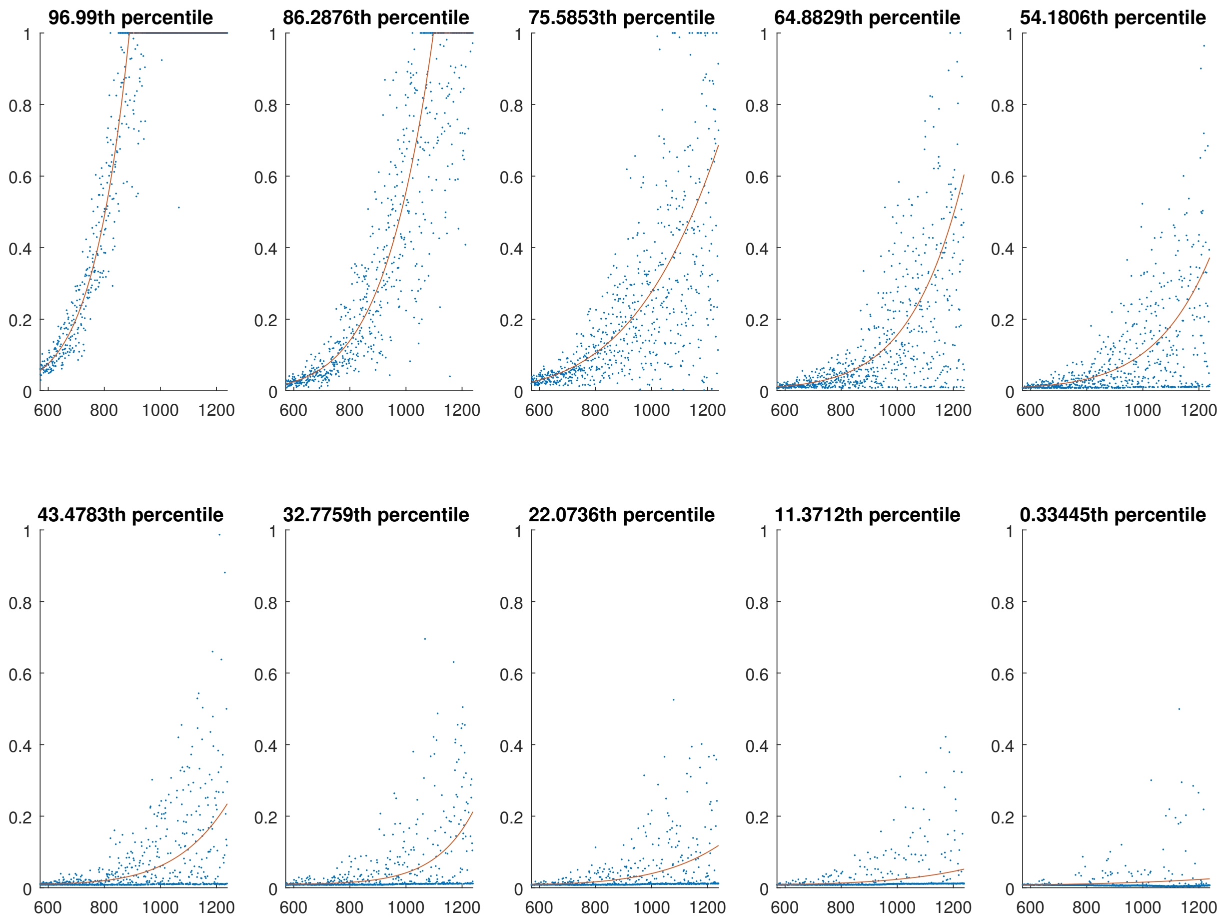

Figure 4.15: Modelling of the observed pixel intensity (blue) through the ML approach outlined by equations (3.6) and (3.7) for a few different percentiles of average pixel intensity. The 7 parameter ML model given by eq. (3.15) has been used. The model has been applied to the dataset *pmt_3_trunc*.

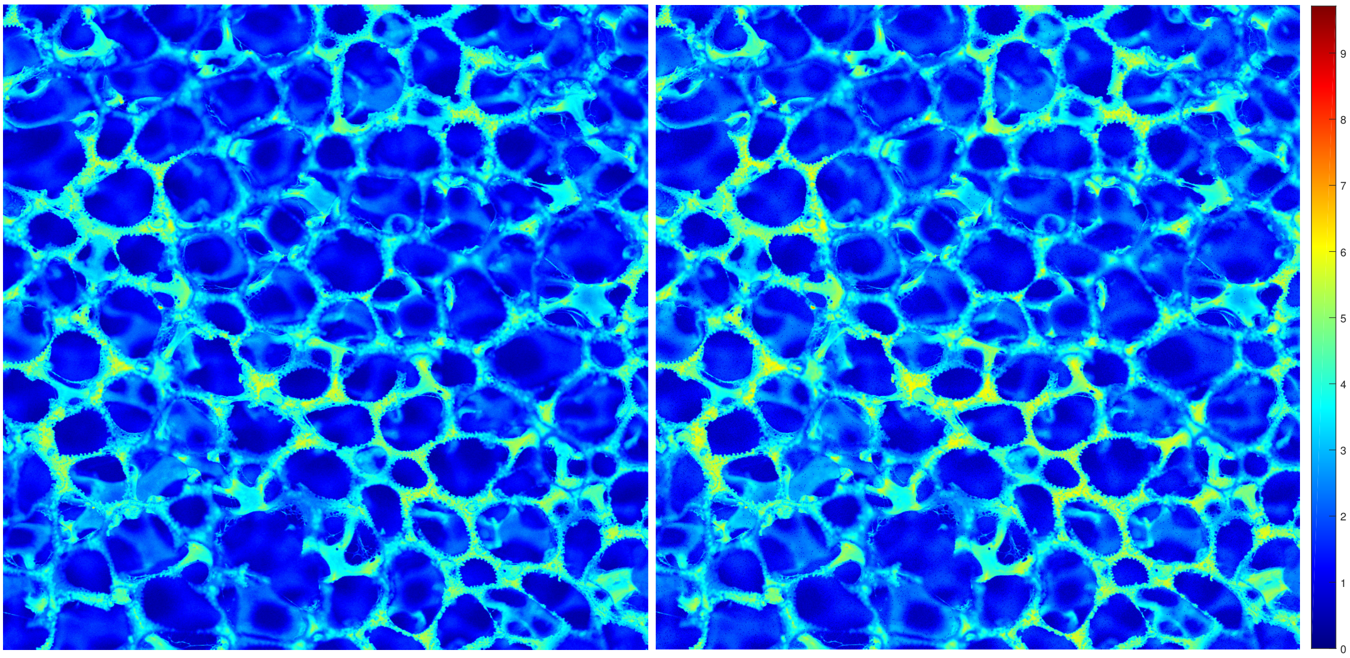

Figure 4.16: The image obtained through the use of the LS method (left, this is the same image as the left image in Figure 4.9 but with another colorscale). The image obtained through the use of the 7 parameter ML model eq. (3.15) (right). The images are tone mapped using a logarithmic operator and subsequently shifted such that the lowest recorded intensity is 0 in each image. The images are taken from the dataset *pmt_3_trunc* and simulate a gain of 850.5 V.

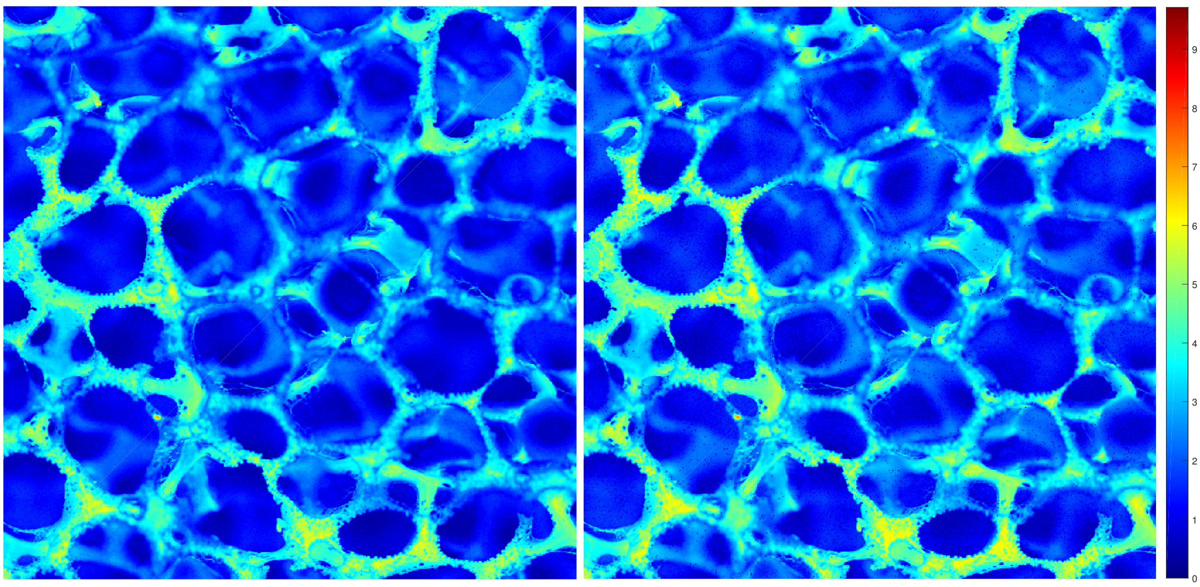

Figure 4.17: Zoom-in of an area of Figure 4.16, both subfigures display the same area.

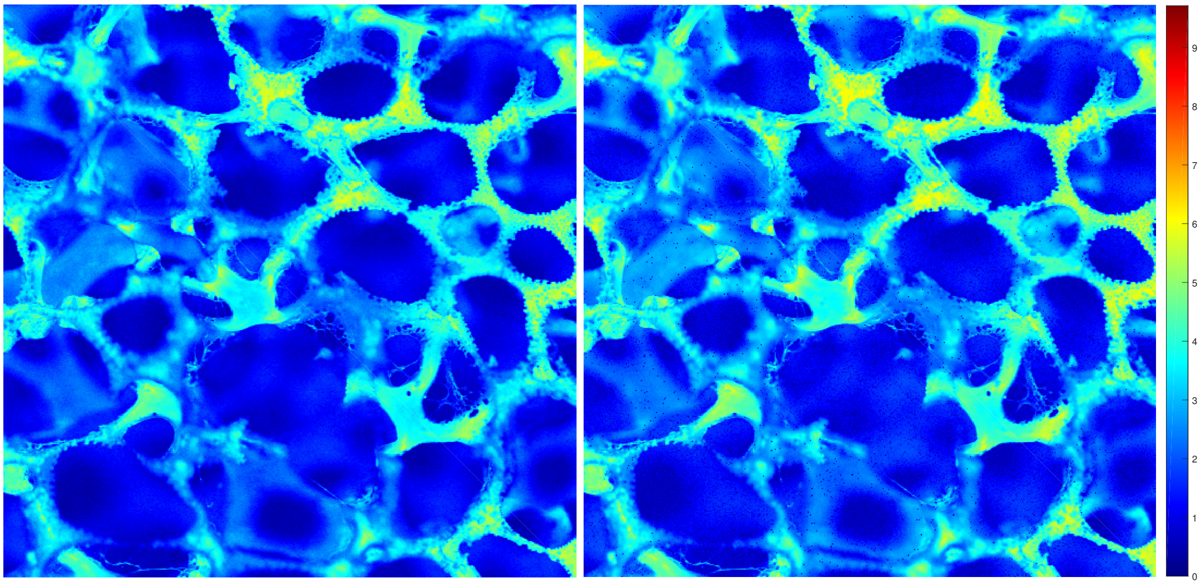

Figure 4.18: Zoom-in of an area of Figure 4.16, both subfigures display the same area.

Although computational time is not a primary concern, it's still interesting to note that there are large differences in the amount of cpu time required to estimate the coefficients of the different models. For the LS model, roughly 14 hours of cpu time (single core of an Intel i5-4570 at 3.2 GHz) is needed in order to estimate the coefficients based on the 700 images of dataset *pmt_3_trunc*. When using the ML model eq. (3.15), for the same dataset, roughly 27 500 hours of cpu time (running on an AMD Opteron 6220 1.4 GHz) is needed. It should be noted that since the model parameters in both cases are estimated individually for every pixel it is very straightforward to parallelize the code.

The likelihood function is optimized using a built-in MATLAB routine called `fmincon`. This routine can be used to solve very general forms of constrained optimization problems and is, as most routines used to numerically solve optimization problems, very sensitive to the initial point which is used to solve the problem. Since we in the general case have limited prior knowledge of the range of plausible parameter values the optimal parameter values might lie, the initial point is chosen to be a vector of uniformally distributed random values. Due to the sensitivity of the initial guess we have to perform many iterations for each pixel, where one iteration is a random initialization of the optimization routine. When computing the parameters which ultimately were used to create the right image of Figure 4.16, 450 iterations were performed for each pixel. The reason why a static number of iterations has to be chosen instead of e.g. iterating until some termination criteria is met is because it is impossible to construct a reasonable termination criteria. Since the likelihood value is only determined up to a multiplicative constant, it can only be used to compare the fit between two choices of model parameters - it can never provide an absolute measurement of the level of fit provided by the particular choice of model parameters. As such, it's not a suitable quantity to use in a termination criteria.

The use of a static number of iterations means that there is potentially too few iterations run for certain pixels, meaning that a satisfactory solution might not be found. By carefully examining Figures 4.17 and 4.18 we note that for the ML model there is a bit of so called pepper noise present in the form of some pixels having a pixel value which is much smaller than their nearest neighbours. When plotting the fitted $I(x, \hat{\boldsymbol{\theta}})$ for these pixels it is clear that the optimization routine hasn't found a solution which is close to a global optimum and has instead found a solution which underestimates the value of $I(x, \boldsymbol{\theta})$, which is why the pixel is so dark compared to its neighbours. When some additional iterations are run we obtain a solution which fits the observed data better and which generates an estimated pixel value which better fits the pixel's immediate neighbourhood. In other words, the suboptimal fit for these pixels have to do with the randomness of the initial guesses. It is therefore safe to assume that this pepper noise is due to the practical difficulties of solving the proposed model and not because the model in itself performs poorly. With a static number of iterations there is also the possibility of running an excessive amount of iterations for certain pixels which means that computational time is effectively wasted. If a proper termination criteria existed it would thus be possible to obtain a result which not only has less noise but also requires less computational time to obtain.

4.2.2.2 The 3 parameter model

The 3 parameter ML model was sought for on the basis of speeding up the solving of the ML model as well as reducing the correlation between parameters and thus avoiding overfitting the model. This reduced model takes the form $I(x, i) = \alpha_i e^{\beta_i (x'(\delta) - x_0)}$, $\sigma^2(x, i) = a_i e^{bx}$ where α_i, β_i and a_i are fitted individually for each pixel and $\delta = 0.18$, $x_0 = 13.69$ and $b = 0.02$ are constants which were estimated prior to the estimation of α_i, β_i and a_i. This section displays the results obtained for primarily 3 datasets: *wheat_bran*, *emmer_wheat* and *foam*. Some additional results can be found in Appendix A.

As seen when comparing Figures 4.19 and 4.20 there is virtually no difference in terms of accuracy between the 7 parameter model and the 3 parameter model. Note that the predetermined parameters (δ, x_0 and b) only needs to be estimated once and can then be used for other datasets with good results, as shown in Figure 4.21. The 3 parameter model also has the added benefit that the minimum number of observations (images) needed in order to fit the model is lower than for the 7 parameter model as more parameters mean that more observations are needed. Decreasing the number of LDR images needed will not only speed up computations but also make the method more applicable for samples which are sensitive to photobleaching as the total time for capturing the images is reduced.

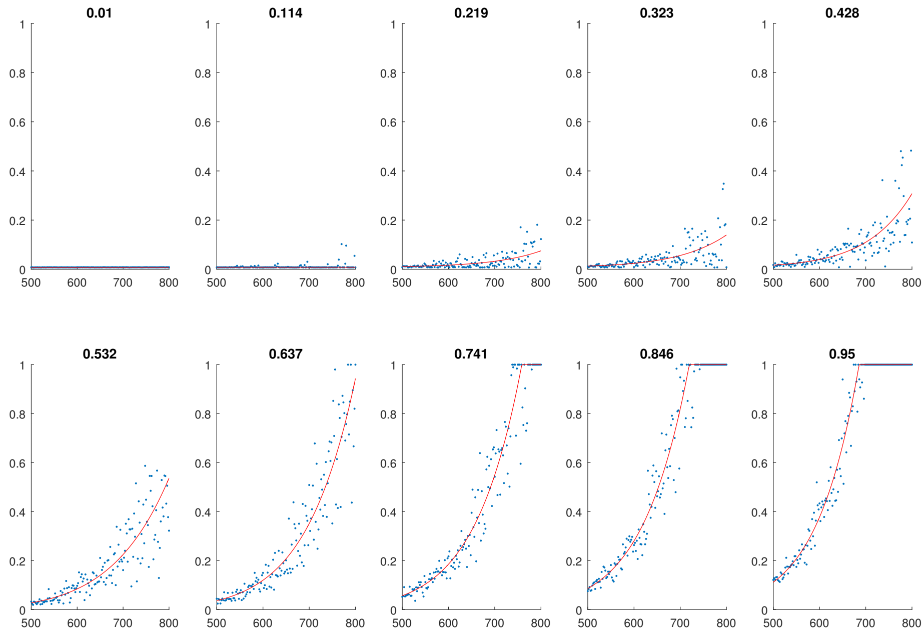

Figure 4.19: Results when using the full model given by eq. 3.15 (7 parameters fitted for each pixel): $I(x,i) = \alpha e^{\beta(x'(\delta)-x_0)} + \gamma$, $\sigma^2(x,i) = ae^{bx}$. Data comes from the dataset *pmt_wheatbran*.

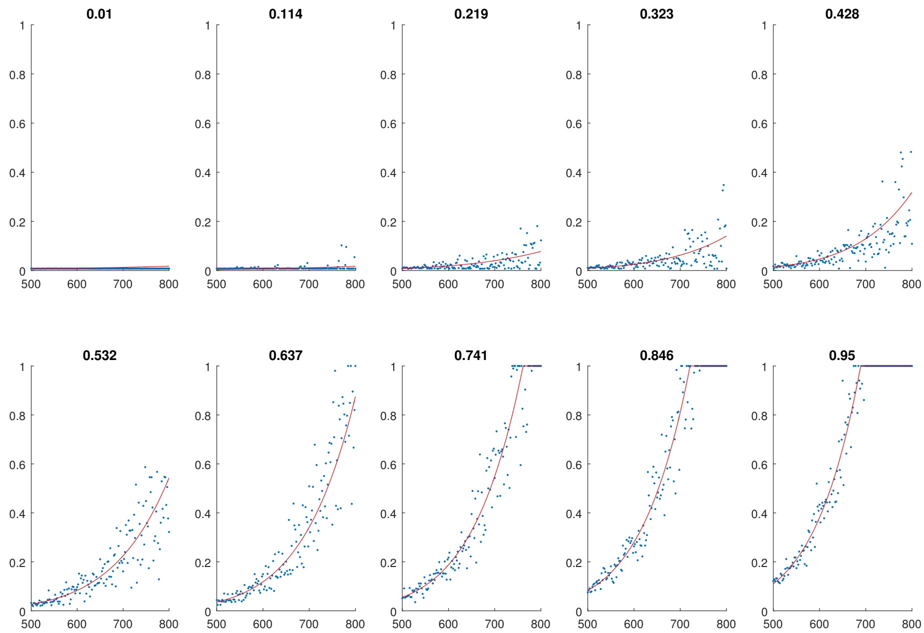

Figure 4.20: Results for the same data shown in Figure 4.19 when using the reduced model give by eq. 3.16 (3 parameters fitted for each pixel).

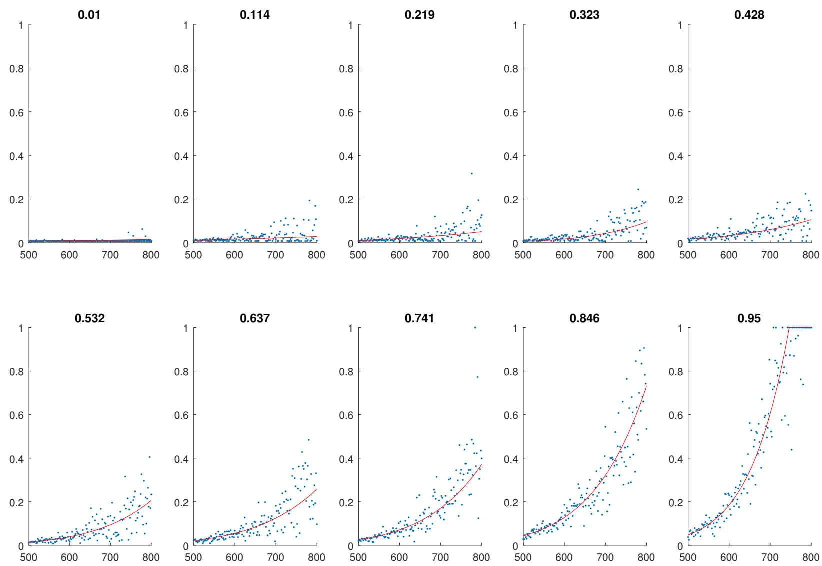

Figure 4.21: Results when applying the model used in Figure 4.20 (using the same values for the constant parameters) to a different dataset, *emmer_wheat*.

As noted in Figure 4.3 and the surrounding text the LS method is typically the least accurate for low gains. This is further is exemplified in Figure 4.22 which shows that the ML method performs much better in this gain region and is able to distinguish between background (air) and sample (foam).

The accuracy of the estimated pixel intensity predicted by the model can be further investigated by applying the method to artificially censored data. To this end we pick a number of random pixels and choose a threshold less 1. For each observed pixel value which is greater than the threshold value, we set the observed value to be equal to the threshold value. This means that we're effectively simulating what would have been observed if a sensor with reduced dynamic range had been used to capture the images. The artificially censored data is then used to estimate the true pixel intensities using the 3 parameter ML model. We can then compare the fit for the artificially thresholded data to the original data in order to see how accurately the ML model predicts the censored values. The results of this test can be found in Figures 4.23 and 4.24. In particular, Figure 4.24 shows that the model is able to accurately predict the artificially censored values which means that the model should also be able to accurately predict the true values of the (not artificially censored) observed data.

For an accurate model Figure 4.23 should contain straight lines which ideally are quite thin for larger values of the threshold but grows wider the more the threshold is increased (meaning that more and more data is censored). Since the data is quite noisy we will in practice not observe a thin, straight line as even though the estimate model fits data well there will always be observations which lie quite far from the estimated curve. It should be noted that for these figures we have restricted

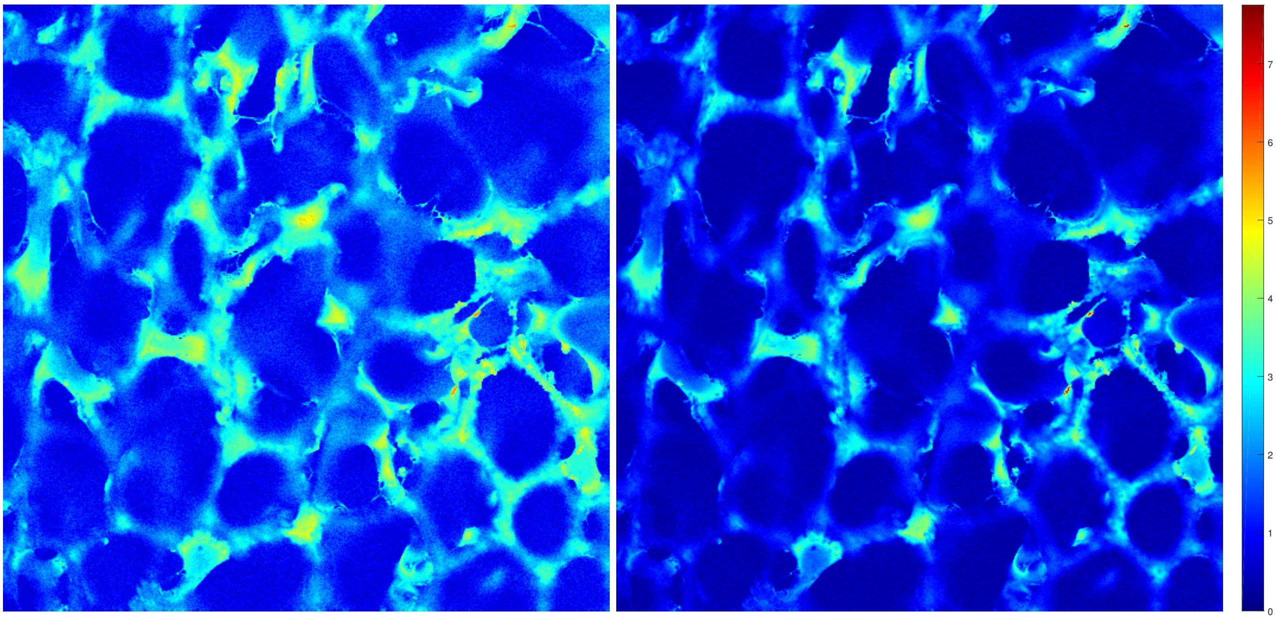

Figure 4.22: The image obtained through the use of the LS method (left). The image obtained through the use of the 3 parameter ML model (right). The tone mapping of the images is based on the right image: the axis scale is obtained by taking the logarithm of the estimated values and subsequently linearly shifting all values such that the lowest value is 0. The images are taken from the dataset *foam* and simulate a gain of 600 V (the lowest gain used when capturing the images).

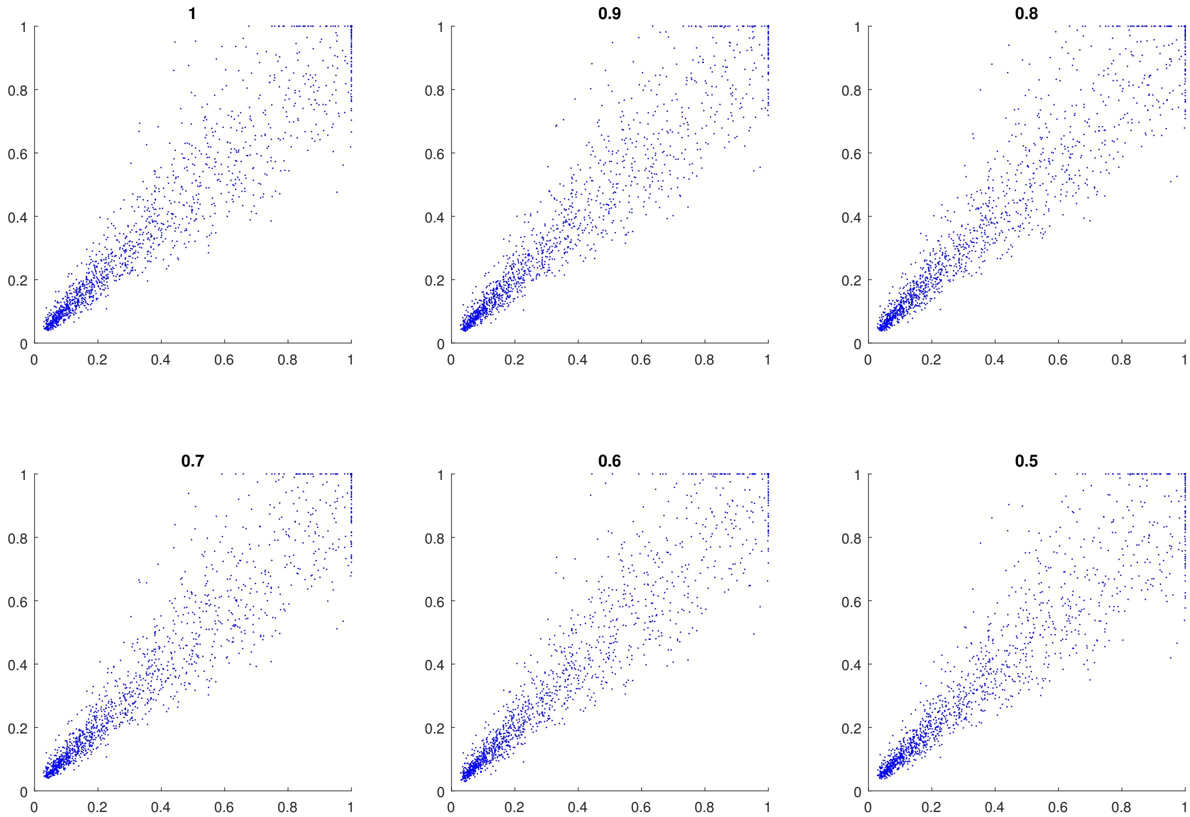

Figure 4.23: Scatter plot of the results obtained when applying the 3 parameter ML model on dataset *pmt_emmer_wheat* where different artificial thresholds have been introduced. The x-axis denotes the observed (not artificially censored) intensity values and the y-axis denotes intensity value which has been estimated based on the artificially censored data. Note that it is the minimum of the estimated intensity and 1 which is plotted since the observation are censored at 1. The threshold used is noted above each subfigure.

ourselves to picking pixels which have relatively high average intensity in order to consider data which is actually affected by the artificial threshold introduced. A pixel with low average intensity will be unaffected by the artificial thresholding and is thus not of interest for this procedure.

Although the 3 parameter ML model is faster to solve than the 7 parameter model, it is still much slower than the LS model. For the LS model, roughly 2.4 hours of cputime (single core of an Intel i5-4570 at 3.2 GHz) is needed in order to estimate the coefficients based on the 150 images of dataset *wheat_bran*. When using the 3 parameter ML model, for the same dataset, roughly 1680 hours of cputime (running on an AMD Opteron 6220 1.4 GHz) is needed to complete 400 iterations. For the same model and dataset it takes roughly 205 hours to complete 50 iterations (running on the same AMD Opteron 6220 1.4 GHz) and a comparison between the results can be found in Figure 4.26. From this figure we note that although running 50 iterations instead of 400 iterations results in an image which has some regions with more noise, the overall appearance of the images are quite similar and there doesn't seem to be any major loss of details present. The reason why different processors were used for the LS and the ML model is the fact that the LS model can be solved in reasonable time on a standard desktop computer whilst the ML model is better handled by a computer cluster, which had different hardware.

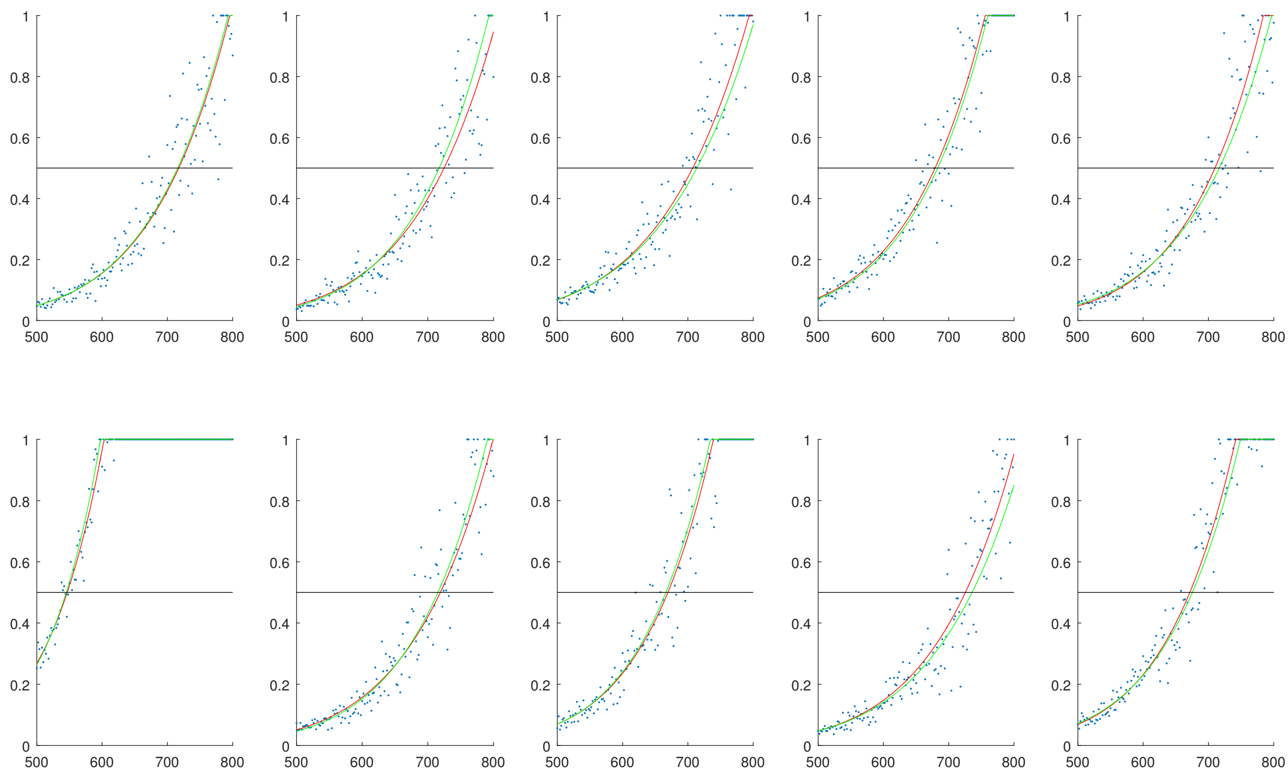

Figure 4.24: Results of applying the 3 parameter ML model to data which is censored at the threshold (0.5) marked by the black line (this figure is an alternative representation of the data shown in the bottom-right subfigure of Figure 4.23). The fitted curve (green line) which is estimated from the artificially censored data is a good fit to the observed (not artificially censored) data (blue dots) and is also close to the curve fitted to the observed data (red line).

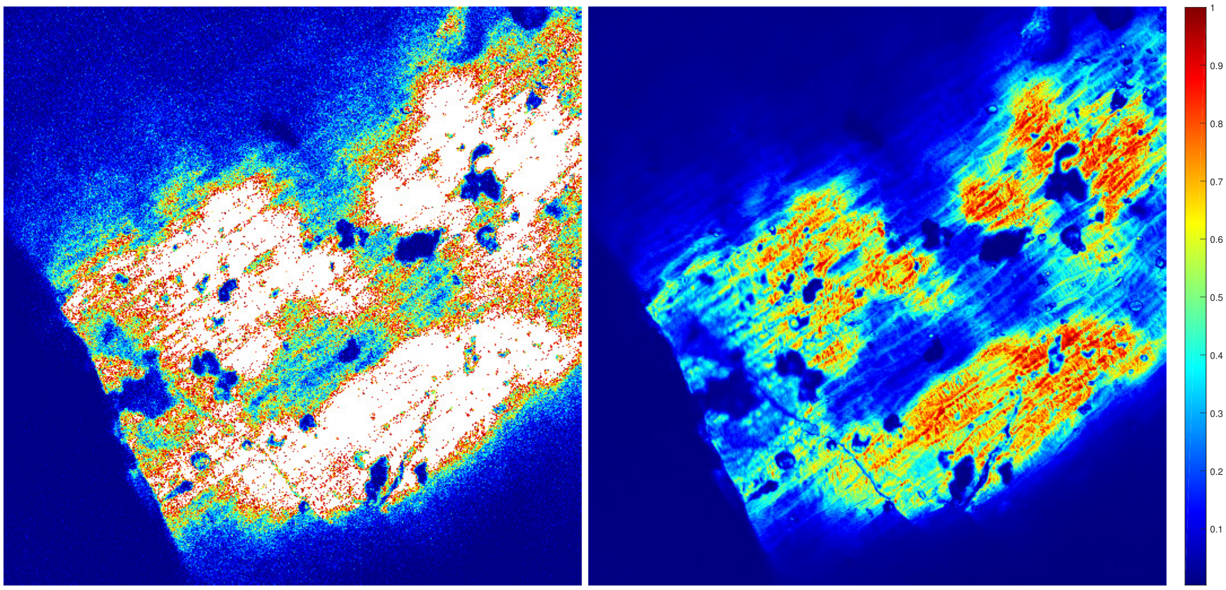

Figure 4.25: The original image captured using the microscope (left, same images as the left image of Figure 4.12). The image obtained through the use of the 3 parameter ML model (right). Both images use the same color axis where 1 represents the largest intensity (marked with white color). Note however that these pixel values are normalized by the largest value in each respective image and as such the values are only comparable in the relative sense and not in the absolute sense. The images are taken from the dataset *wheat_bran* and simulate a gain of 752 V.

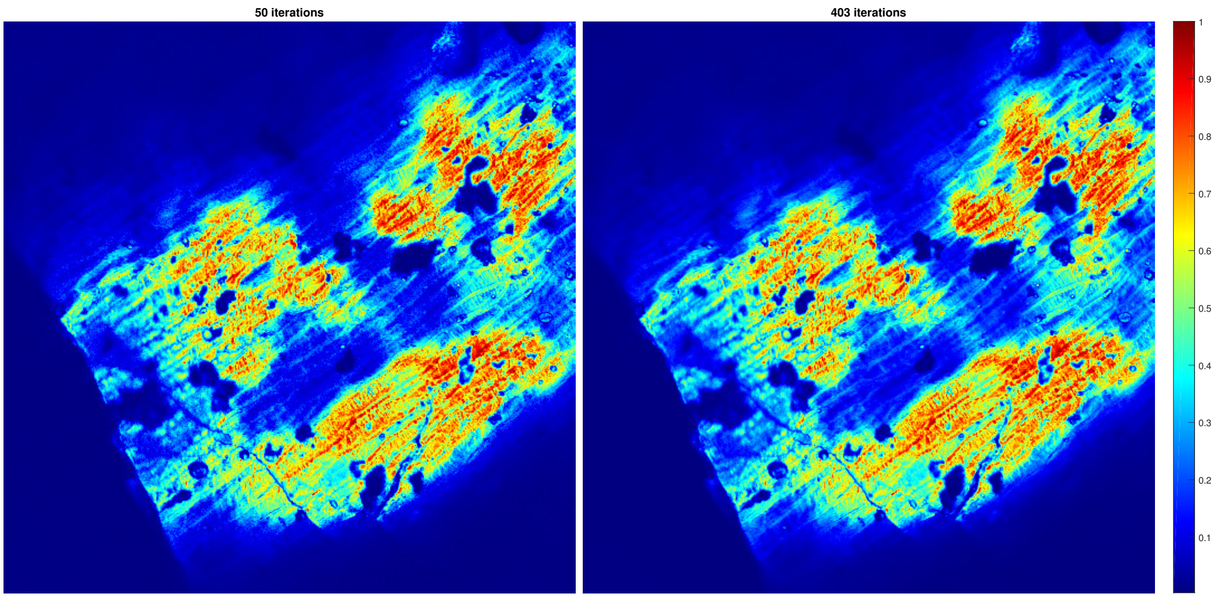

Figure 4.26: Same scenario as that shown in Figure 4.25. Results after 50 iterations (left) compared to the results after 403 iterations (right, same image as the right subfigure of Figure 4.25) using the 3 parameter ML method.

5

Conclusion

Two methods for constructing HDR images based on several LDR images has been proposed: the LS method and the 3 parameter ML method. The proposed methods have been shown to produce HDR images which do not have any saturated pixel values and contain less noise than their LDR counterparts. As such, the constructed HDR images contain more accurate information about the sample at hand and for some of the tested datasets the HDR images reveal details about the studied material which were not visible in the original LDR images. The methods have been successfully applied to several different types of samples which shows that it is applicable for imaging of a wide variety of materials.

The proposed ML model generally fits data better than the proposed LS model. The two main reasons for this is that the ML model doesn't assume constant variance and that a likelihood model for censored data better models the saturation of pixels than simply applying the minimum operator, as is done in the case of the LS model. On the other hand, this makes the model more complicated and it is considerably more computationally expensive to solve. In its current state the ML model will in some situations be too expensive to solve within reasonable time on an average desktop computer and instead requires a more powerful setup such as a computer cluster. As such, there are some things concerning this work which could be improved upon.

The LS model is solved using a built-in MATLAB routine (`nlinfit`) which performs iterative nonlinear LS in order to estimate the model coefficients. This problem is of a much less general nature than optimizing an arbitrary function as `fmincon` does and as such this routine utilizes a more highly specialized and efficient algorithm in order to perform the computations. A potentially large speed-up of the computation time for the ML method could thus be reached by writing a more specialized algorithm for solving the optimization problem. As the LS routine is not nearly as sensitive to the starting guess as the optimization routine is, it has for all tested cases always been enough to run a single iteration in order to obtain a reasonable solution. The ML model, on the other hand, requires several iterations in order to obtain a reasonable solution. It might be possible to reduce the number of iterations required by finding smaller subdomains of the feasible parameter space to which the initial guesses could be restricted.

Although the proposed ML models fits data well there is no known physical interpretation of the model parameters. The validity of the model could thus be further verified if it were possible to find a connection between the model parameters and some property of the microscope and/or the sample. If a physical interpretation was available the numerical parameter values by themselves would provide valuable information about the sample, thus increasing the amount of information which could be obtained through the proposed method.

Throughout this work a fundamental assumption has been that the movement of a sample is negligible between images and thus that the sample can be considered to be fully static. If this is not the case, i.e. if it is desirable to capture scenes where movements occur, some form of movement compensation technique would need to be utilized before the parameter estimation procedure is carried out. The development of such a technique would broaden the area of application of the proposed method.

The constant parameters δ, x_0 and b of the 3 parameter ML model were fit based on a single dataset and then found to be applicable for all other datasets tested. However, one could possibly obtain better estimates of these parameters by simultaneously fitting the parameters for data coming from several different datasets. These parameter estimates would presumably be better in the sense that it would be easier to find good estimates of the remaining 3 (pixel-dependent) parameters, potentially increasing the accuracy of the model slightly but primarily making it faster to solve.

Bibliography

[1] R. Borlinghaus, "Sensors and measuring techniques in confocal microscopy," *Leica Microsystems Technological Readings*, 2015.

[2] S. Mann and R. W. Picard, "On being 'undigital' with digital cameras: Extending dynamic range by combining differently exposed pictures," in *Proceedings of IS&T*, pp. 442–448, 1995.

[3] P. E. Debevec and J. Malik, "Recovering high dynamic range radiance maps from photographs," in *Proceedings of the 24th Annual Conference on Computer Graphics and Interactive Techniques*, SIGGRAPH '97, (New York, NY, USA), pp. 369–378, ACM Press/Addison-Wesley Publishing Co., 1997.

[4] C. Aguerrebere, J. Delon, Y. Gousseau, and P. Musé, "Best algorithms for hdr image generation. a study of performance bounds," *SIAM Journal on Imaging Sciences*, vol. 7, no. 1, pp. 1–34, 2014.

[5] A. Bell, J. Brauers, J. Kaftan, D. Meyer-Ebrech, A. Böcking, and T. Aach, "High dynamic range microscopy for cytopathological cancer diagnosis," *IEEE Journal of Selected Topics in Signal processing*, vol. 3, no. 1, pp. 170–184, 2009.

[6] A. Adeyemi, N. Barakat, and T. Darcie, "Applications of digital micro-mirror devices to digital optical microscope dynamic range enhancement," *Optics Express*, vol. 17, no. 1, pp. 1831–1843, 2009.

[7] B. Eastwood and E. Childs, "Image alignment for multiple camera high dynamic range microscopy," in *Applications of Computer Vision (WACV), 2012 IEEE Workshop on*, pp. 225–232, Jan 2012.

[8] M. Granados, B. Ajdin, M. Wand, C. Theobalt, H.-P. Seidel, and H. Lensch, "Optimal hdr reconstruction with linear digital cameras," in *Computer Vision and Pattern Recognition (CVPR), 2010 IEEE Conference on*, pp. 215–222, June 2010.

[9] M. Robertson, S. Borman, and R. Stevenson, "Dynamic range improvement through multiple exposures," in *Image Processing, 1999. ICIP 99. Proceedings. 1999 International Conference on*, vol. 3, pp. 159–163 vol.3, 1999.

[10] A. Sohaib and A. Robles-Kelly, "Radiometric calibration for hdr imaging," in

Image Processing (ICIP), 2015 IEEE International Conference on, pp. 2815–2819, Sept 2015.

[11] S. Mann, "Comparametric equations with practical applications in quantigraphic image processing," *Image Processing, IEEE Transactions on*, vol. 9, pp. 1389–1406, Aug 2000.

[12] M. Grossberg and S. Nayar, "Modeling the space of camera response functions," *Pattern Analysis and Machine Intelligence, IEEE Transactions on*, vol. 26, pp. 1272–1282, Oct 2004.

[13] D. Murphy and M. Davidson, *Fundamentals of Light Microscopy and Electronic Imaging.* John Wiley & Sons, 2 ed., 2012.

[14] R. Engstrom and R. Corporation, *Photomultiplier handbook.* RCA Corp., 1980.

[15] M. C. Teich, K. Matsuo, and B. Saleh, "Excess noise factors for conventional and superlattice avalanche photodiodes and photomultiplier tubes," *Quantum Electronics, IEEE Journal of*, vol. 22, pp. 1184–1193, Aug 1986.

[16] K. Kirk and H. J. Andersen, "Noise characterization of weighting schemes for combination of multiple exposures," 2006.

[17] C. T. Ekstrøm, S. Bak, C. Kristensen, and M. Rudemo, "Spot shape modelling and data transformations for microarrays," *Bioinformatics*, vol. 20, no. 14, pp. 2270–2278, 2004.

[18] L. Mandel, "Fluctuations of photon beams and their correlations," *Proceedings of the Physical Society*, vol. 72, no. 6, p. 1037, 1958.

[19] H. H. Tan, "A statistical model of the photomultiplier gain process with applications to optical pulse detection," in *Proceedings of the International Telemetering Conference, San Diego, CA, September 28-30*, pp. 115–122, 1982.

[20] W. Shockley and J. Pierce, "A theory of noise for electron multipliers," *Radio Engineers, Proceedings of the Institute of*, vol. 26, pp. 321–332, March 1938.

[21] V. Zworykin, G. Morton, and L. Malter, "The secondary emission multiplier-a new electronic device," *Radio Engineers, Proceedings of the Institute of*, vol. 24, pp. 351–375, March 1936.

[22] P. M. Woodward, "A statistical theory of cascade multiplication," *Mathematical Proceedings of the Cambridge Philosophical Society*, vol. 44, pp. 404–412, 7 1948.

[23] F. J. Lombard and F. Martin, "Statistics of Electron Multiplication," *Review of Scientific Instruments*, vol. 32, pp. 200–201, Feb. 1961.

[24] J. R. Prescott, "A statistical model for photomultiplier single-electron statistics," *Nuclear Instruments and Methods*, vol. 39, pp. 173–179, Jan. 1966.

A

Results for additional datasets

This section contains the generated HDR images for two additional datasets: *lens_paper* and *toilet_paper*.

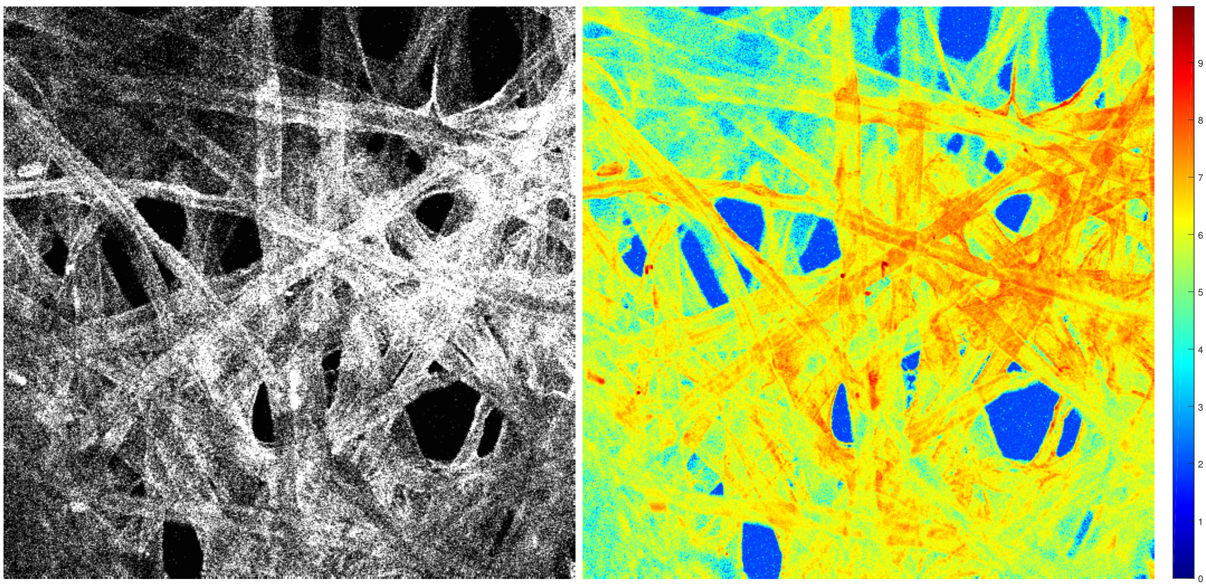

Figure A.1: The original image captured using the microscope (left). The image obtained through the use of the 3 parameter ML model (right). The right image was tone mapped using a logarithmic operator and the values were subsequently linearly shifted such that the minimum intensity is 0. The images are taken from the dataset *lens_paper* and simulate a gain of 1052 V.

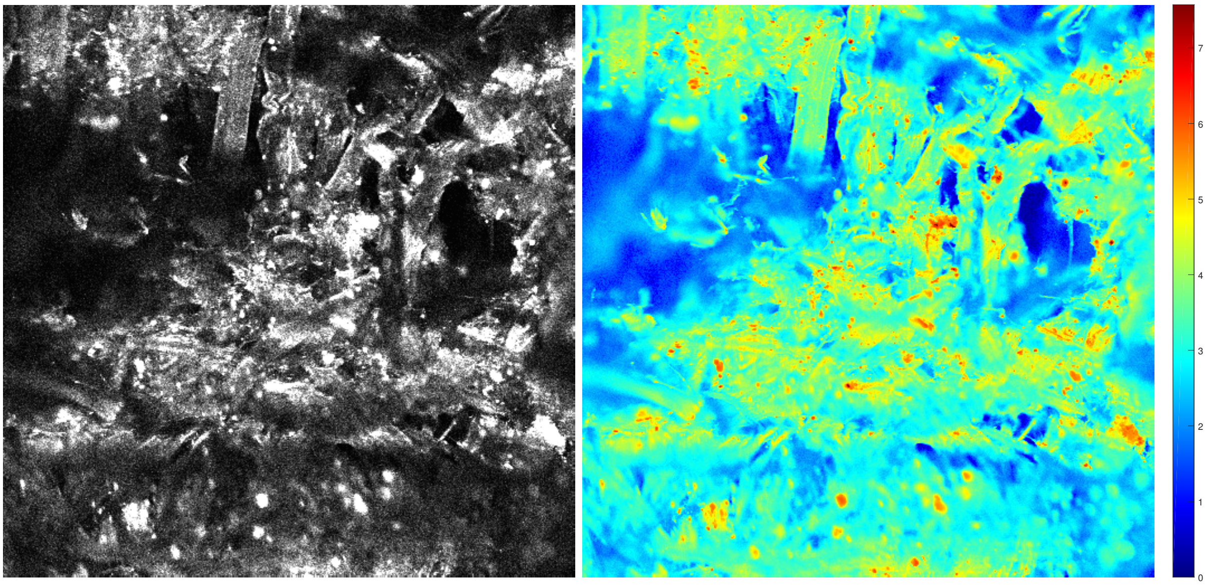

Figure A.2: The original image captured using the microscope (left). The image obtained through the use of the 3 parameter ML model (right). The right image was tone mapped using a logarithmic operator and the values were subsequently linearly shifted such that the minimum intensity is 0. The images are taken from the dataset *toilet_paper* and simulate a gain of 752 V.

B

Images

This appendix contains example images captured using the CLSM.

B.1 *pmt_1*

Dataset contains 250 images captured with the PMT at constant gain.

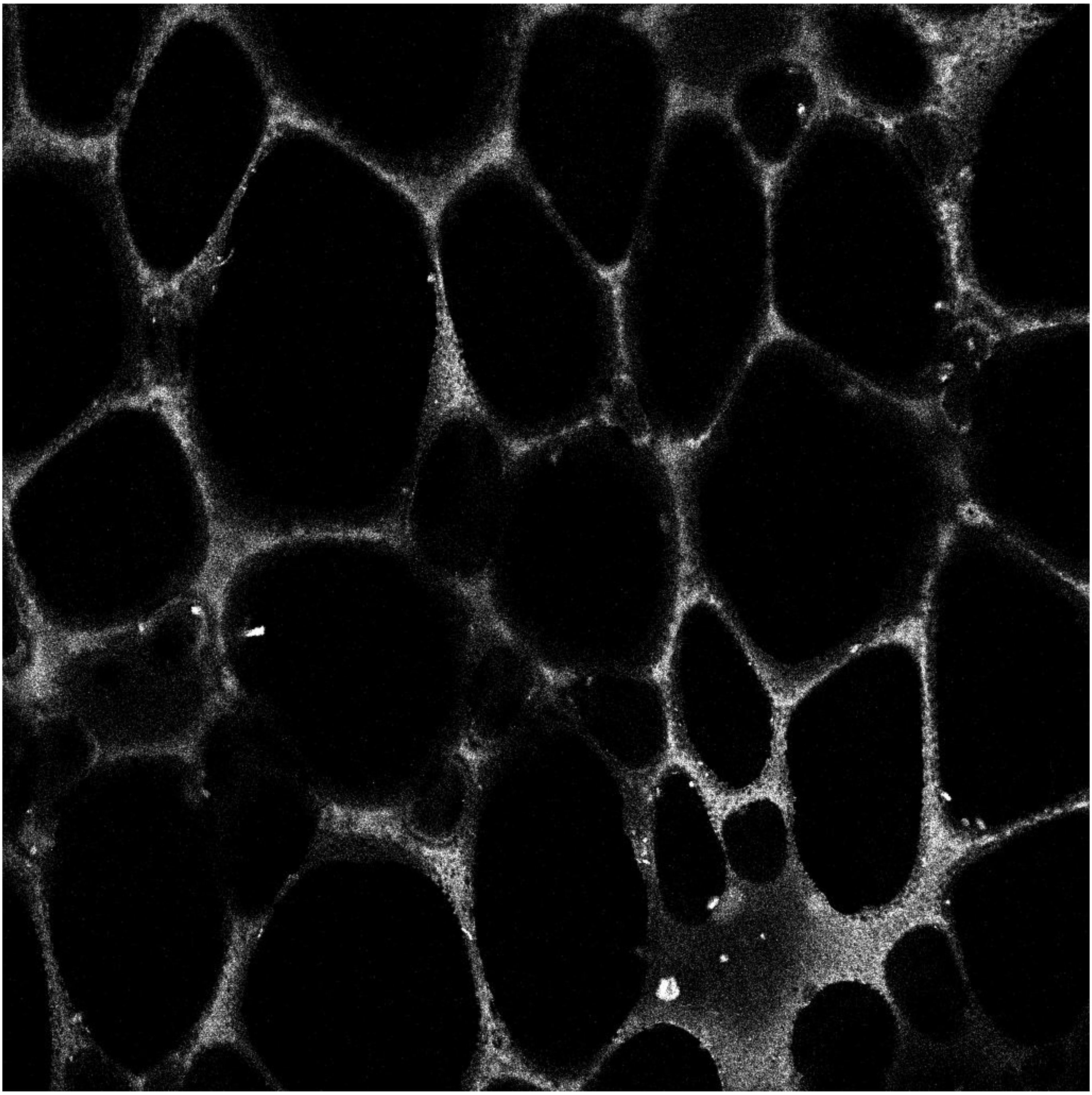

Figure B.1: Image number 1 (first image) of the dataset *pmt_1*.

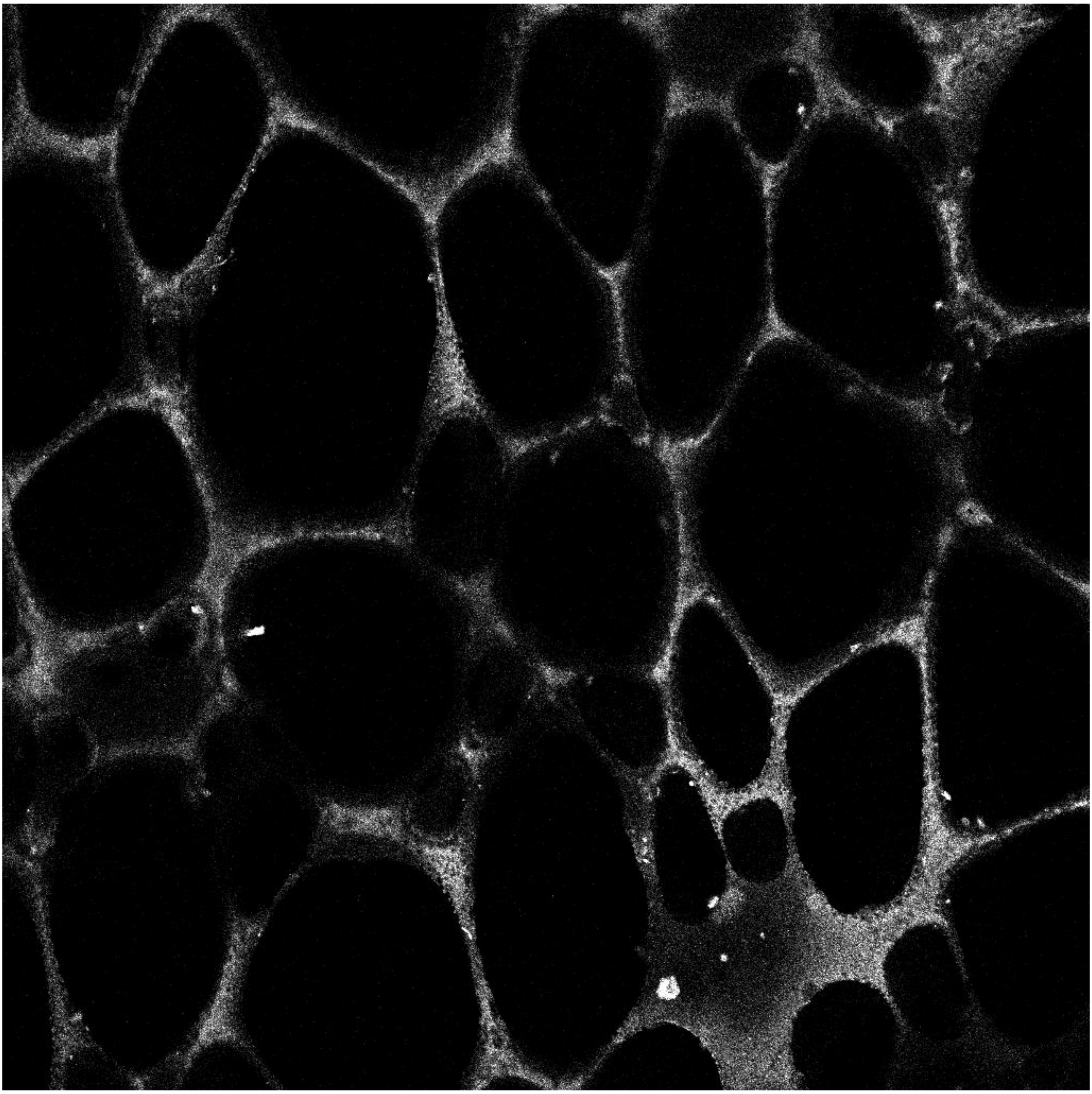

Figure B.2: Image number 125 (image in the middle) of the dataset *pmt_1*.

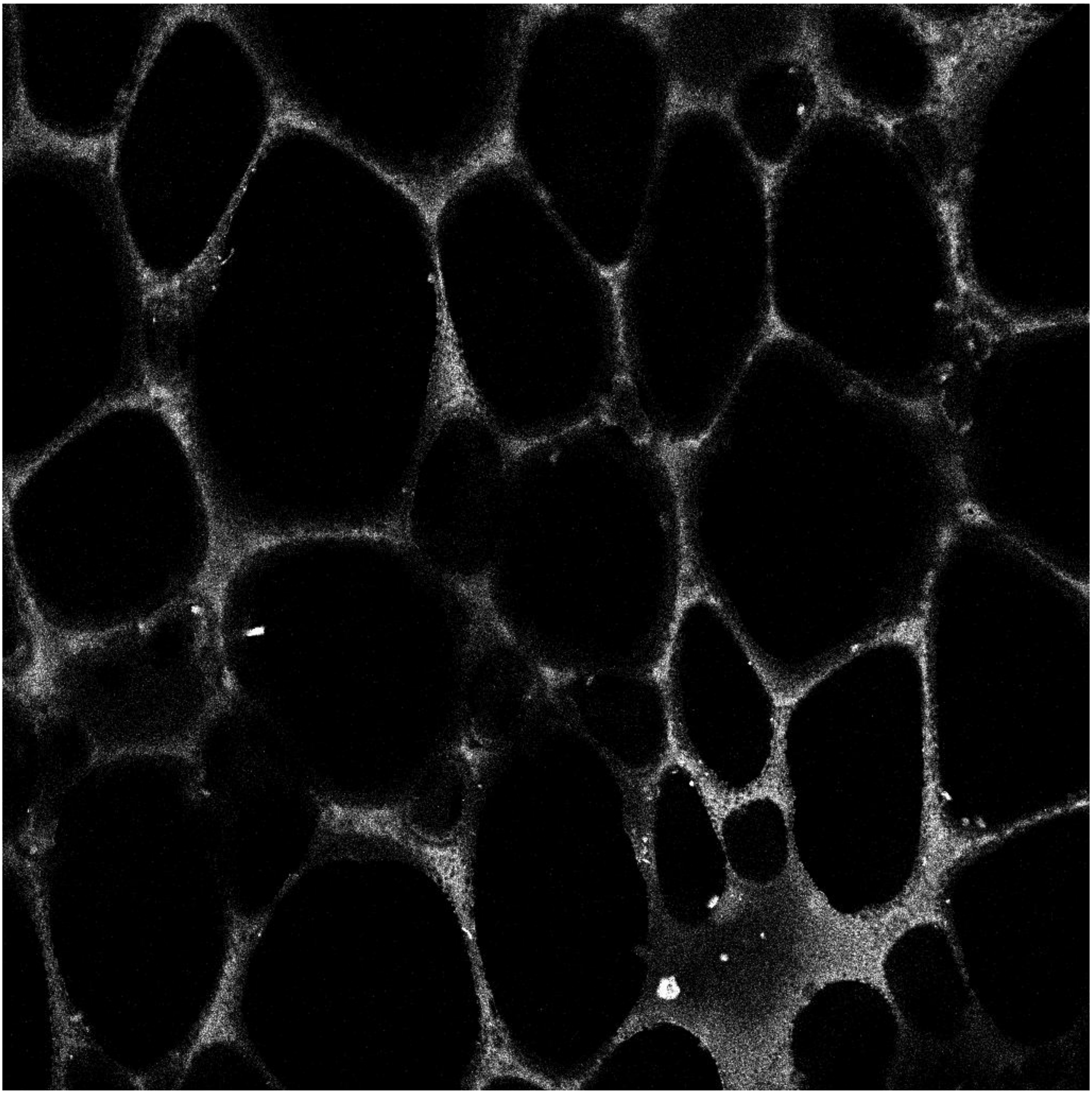

Figure B.3: Image number 250 (last image) of the dataset *pmt_1*.

B.2 *pmt_3*

Dataset contains 1312 images captured with the PMT at varying gain (0 V to 1250 V). The pixels corresponding to percentile 100, 95 and 90 (of average intensity throughout all images) are marked with red, magenta and blue circles respectively. The pixel coordinates are (row, col)=(294, 94), (row, col)=(794, 718) and (row, col)=(315, 85) respectively.

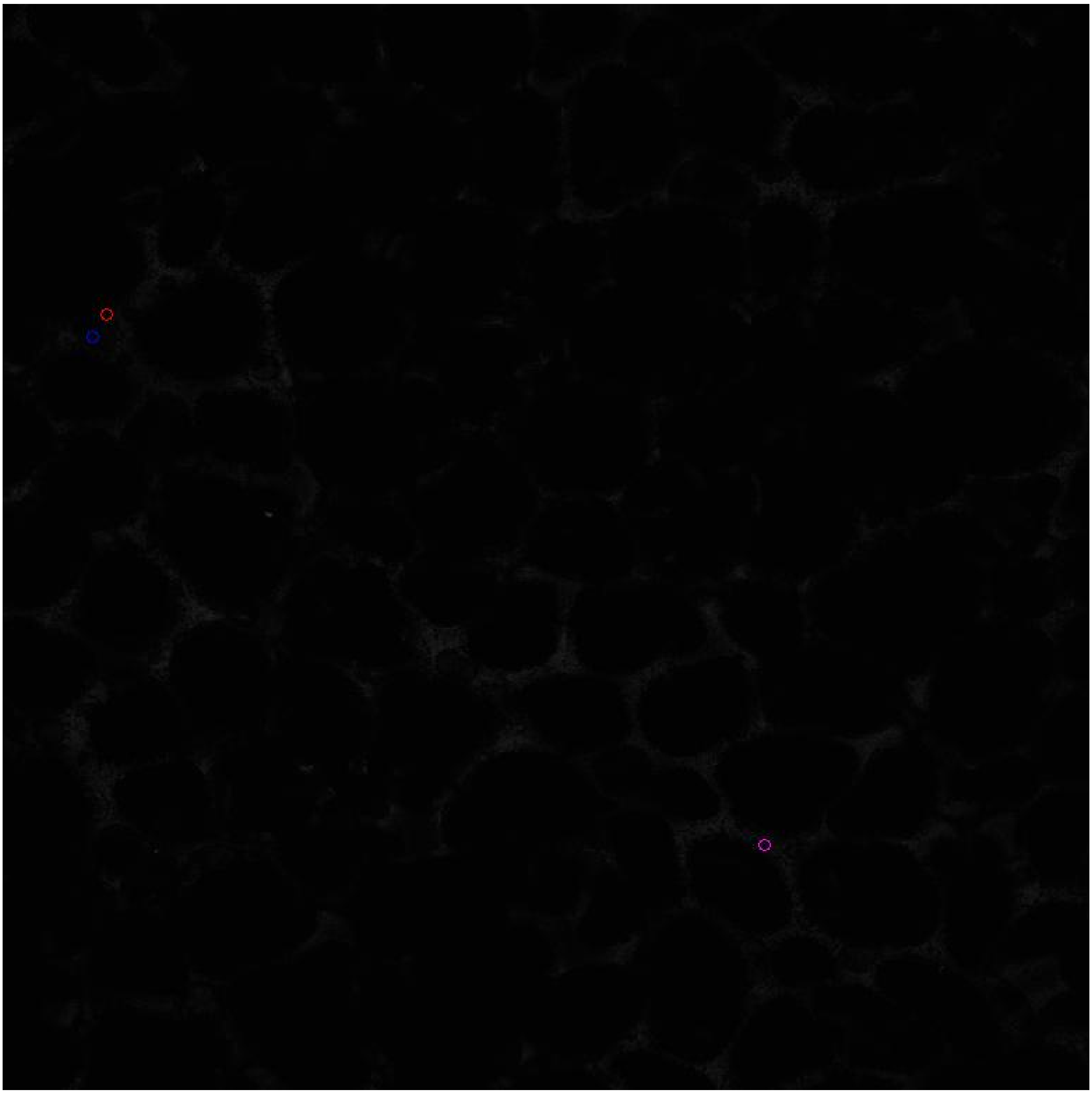

Figure B.4: Image number 550 (images with lower number are more or less completely dark when visualized) of the dataset *pmt_3*. The pixels corresponding to percentile 100, 95 and 90 (of average intensity throughout all images) are marked with red, magenta and blue circles respectively

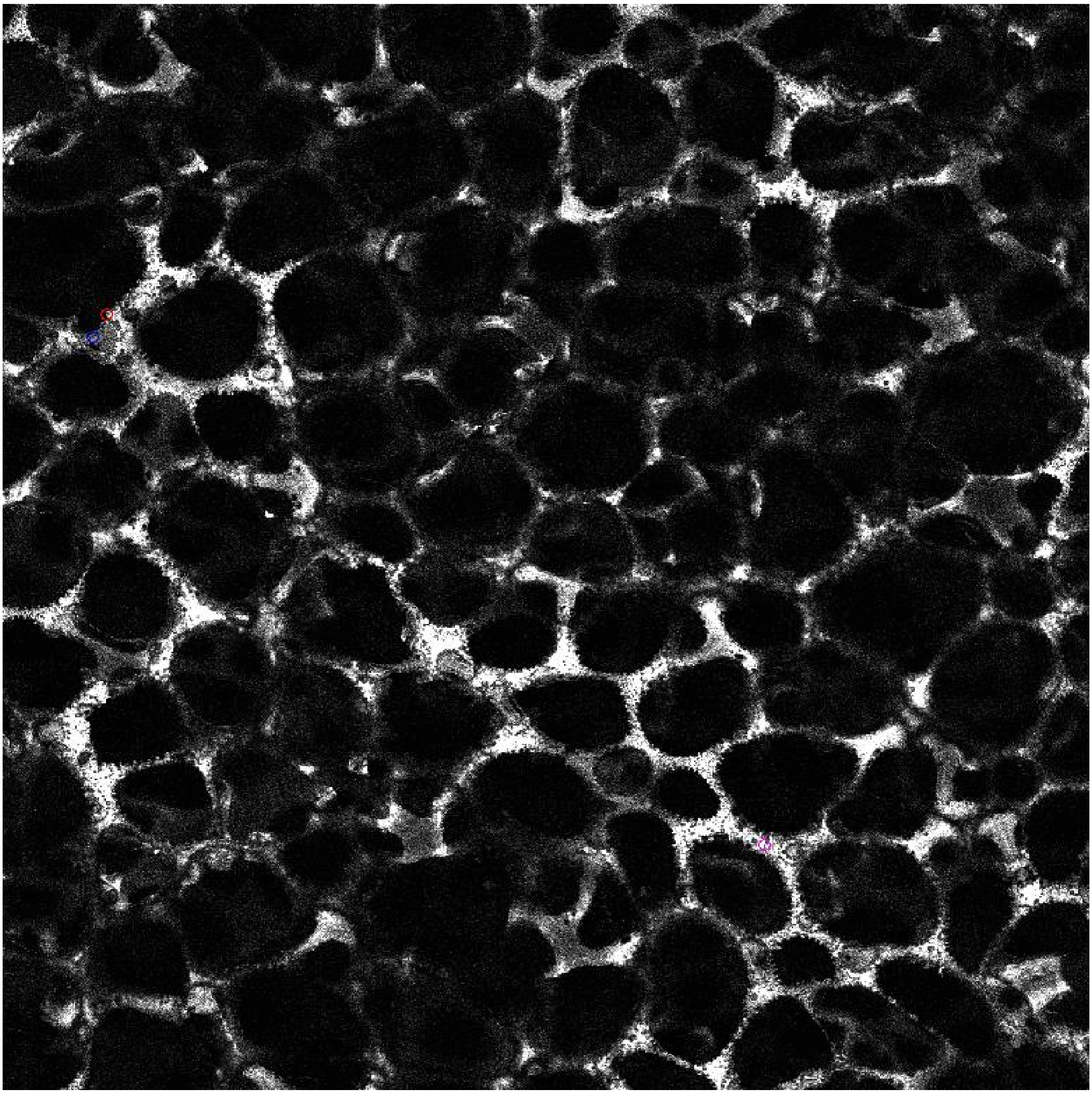

Figure B.5: Image number 900 of the dataset *pmt_3*. The pixels corresponding to percentile 100, 95 and 90 (of average intensity throughout all images) are marked with red, magenta and blue circles respectively

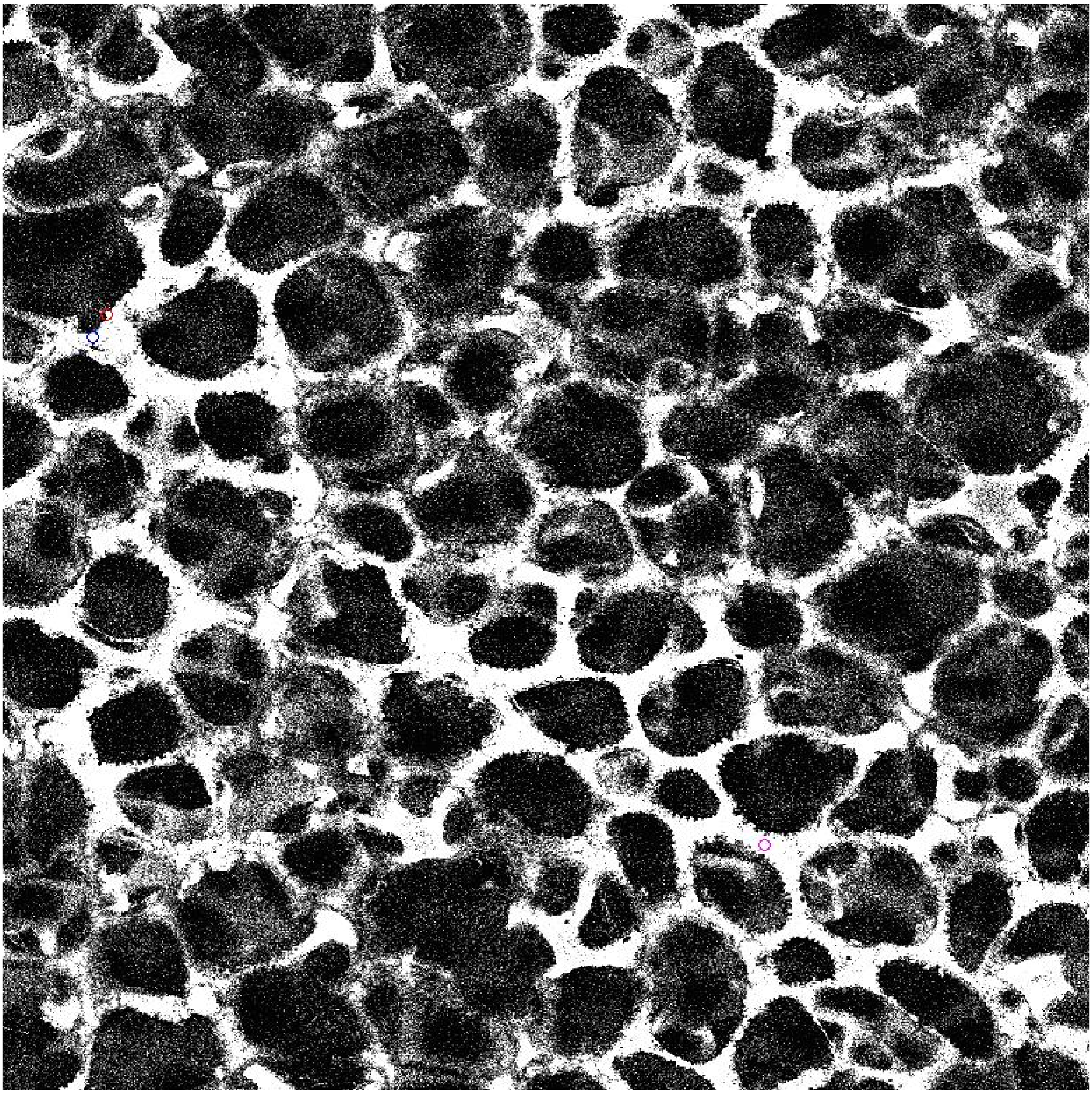

Figure B.6: Image number 1312 (last image) of the dataset *pmt_3*. The pixels corresponding to percentile 100, 95 and 90 (of average intensity throughout all images) are marked with red, magenta and blue circles respectively

B.3 Calibration images

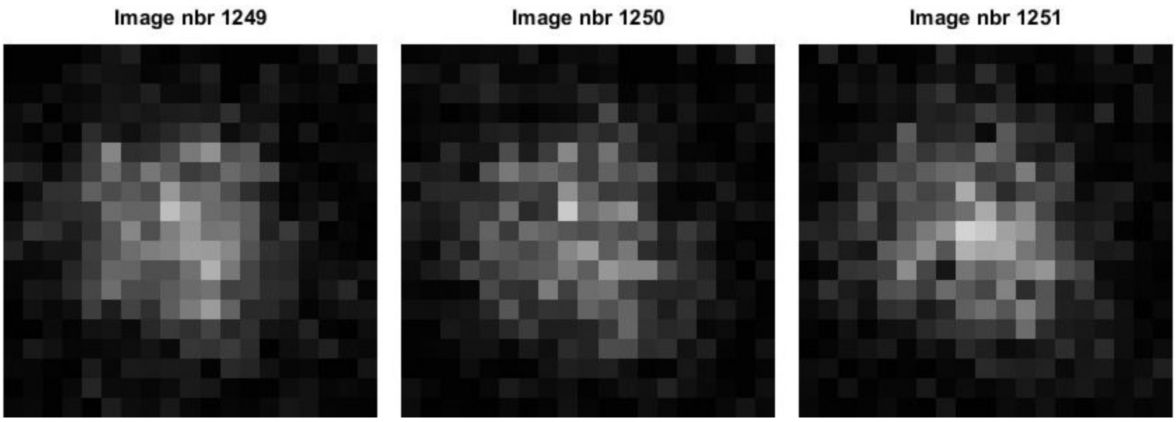

Figure B.7: Zoom-ins of the same area (pixel coordinates) for three consecutive images from the dataset *pmt_4*. Since the microscope settings (gain, physical lengths, resolution etc.) are constant this figures demonstrates the variation of noise between consecutive images.

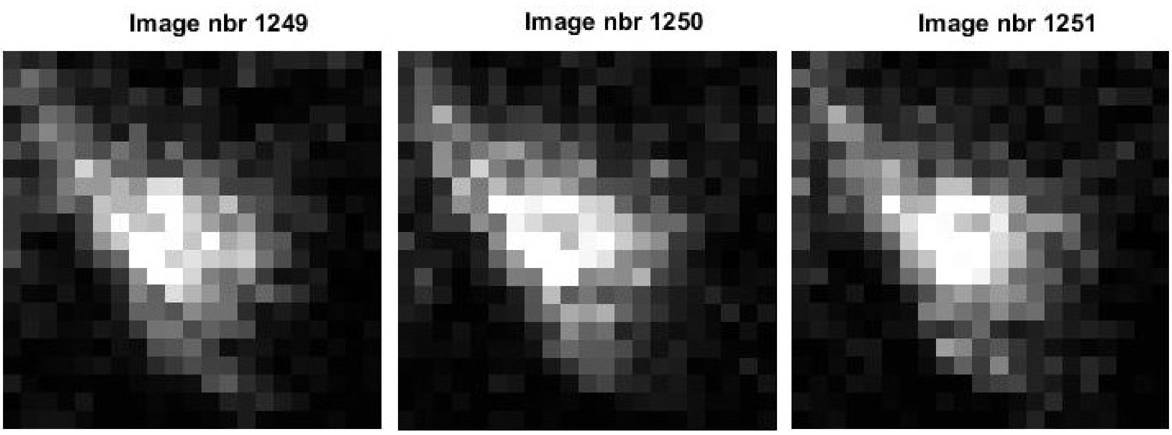

Figure B.8: Same circumstances as in Figure B.7 but for a different area.

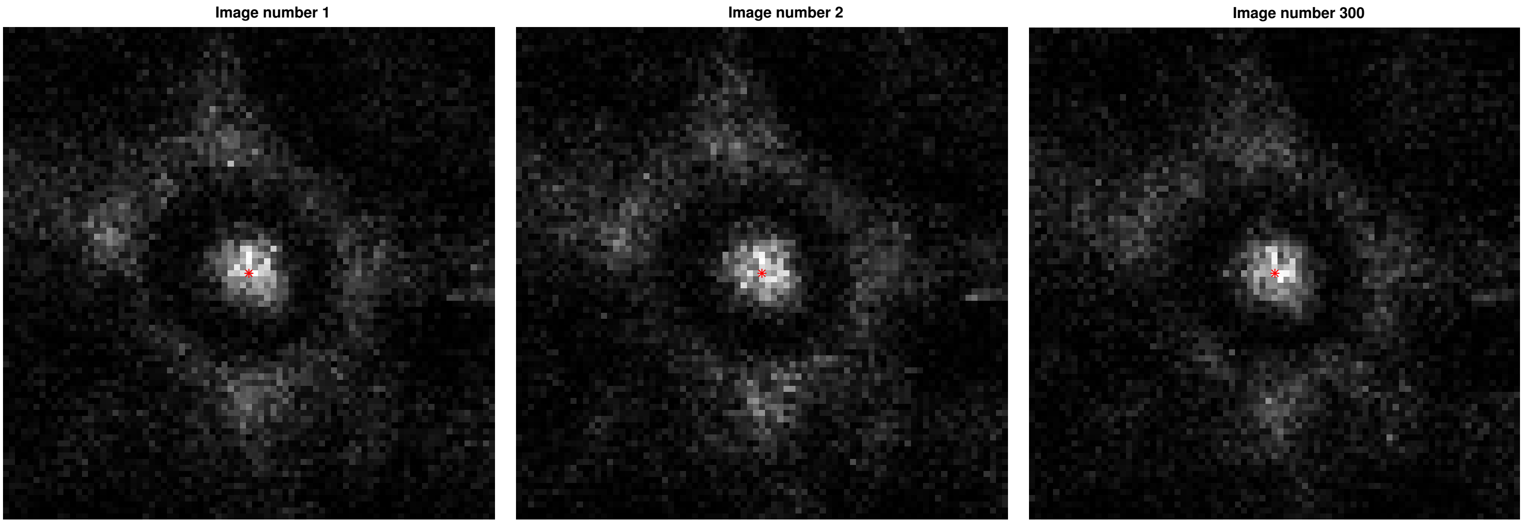

Figure B.9: Zoom-ins of the same area (pixel coordinates) for three images from the dataset *pmt_4*. The center of the images have been marked (red star) in order to make the images more easy to compare.

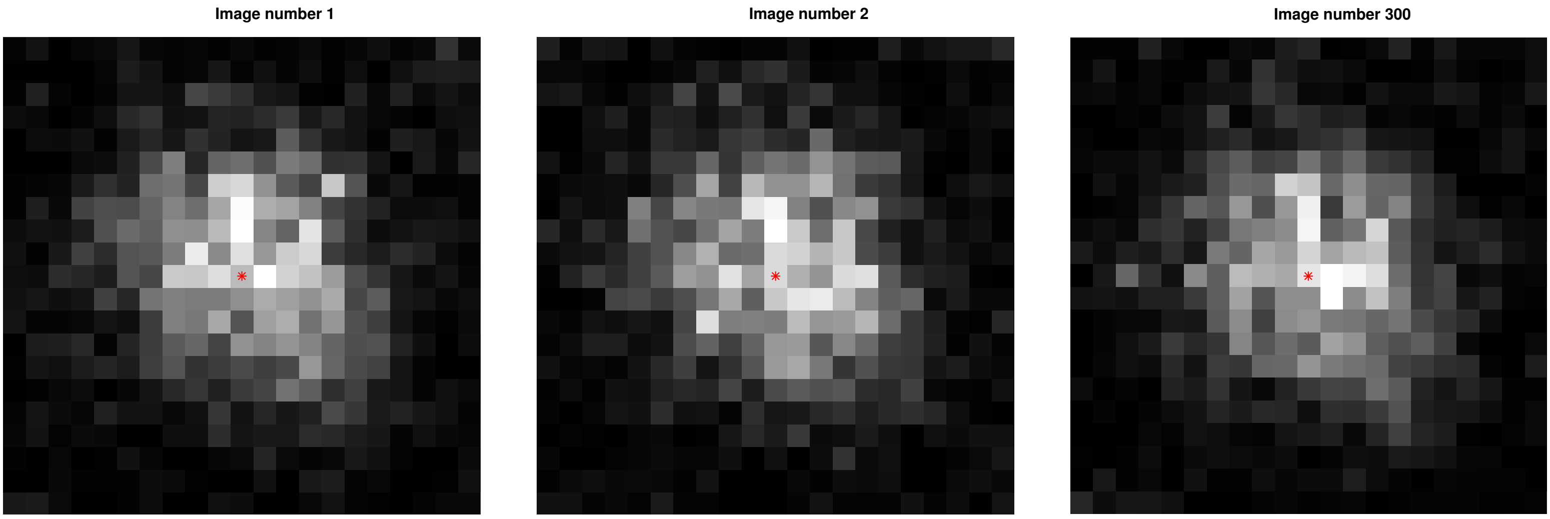

Figure B.10: Zoom-in of Figure B.9.

C

Mathematical theory

C.1 The Poisson distribution

Let X be a discrete random variable. X is said to be a Poisson distributed random variable with parameter $\lambda > 0$ if its probability mass function can be expressed as

$$f(k) = \mathrm{P}(X = k) = \frac{\lambda^k e^{-\lambda}}{k!} \tag{C.1}$$

where k is a non-negative integer. The Poisson distribution gives the probability distribution of the number of events which occur in a fixed time interval, assuming a fixed average rate (λ) and assuming that events occur independently of each other. An important property of a Poisson distributed random variable is that

$$\mathrm{E}[X] = \mathrm{Var}[X] = \lambda \tag{C.2}$$

One way of obtaining an indication on whether or not data might have an underlying Poisson distribution is thus to compute the coefficient of variation $R(X)$ which is defined to be the ratio between the variance and the expected value, viz.

$$R(X) = \frac{\mathrm{Var}[X]}{\mathrm{E}[X]} \tag{C.3}$$

which in theory should be close to one if the data does indeed come from a Poisson distribution.

For a photon counting sensor the number of photons (i.e. the intensity in the captured image) observed during a fixed time frame can in theory be modelled by a Poisson distribution [18]. This implies that for an image captured using a photon counter the observed pixel values can be considered to be a realization of independant Poisson-distributed random variables.

C.2 The Polya distribution

Let X be a discrete random variable. X is considered to belong to a Polya distribution with parameter $0 \leq b \leq 1$ if its probability mass function is given by

$$\mathrm{P}(X = x) = \frac{\mu^x}{x!}(1 + b\mu)^{-x-1/b} \prod_{i=1}^{x-1}(1 + ib) \tag{C.4}$$

where μ is the mean of the distribution. The generating function is given by

$$G(s) = [1 + b\mu(1 - s)]^{-1/b} \tag{C.5}$$

The Polya distribution is also called a compound Poisson distribution and is a special case of the negative-binomial distribution. In the case of a PMT sensor a Poisson distribution has been used to model the individual stages of the multiplication process, e.g. by [19], [20], [21], [22]. However, as observed by [23], experiments show that data typically doesn't agree with the Poisson model but instead more resemble an exponential distribution. Thus an alternative model based on the Polya distribution is sometimes used, for example by [24]. Since the Polya distribution has both the Poisson distribution ($b = 0$) and the geometric distribution ($b = 1$) as special cases it is a suitable alternative to the Poisson distribution in the case of a PMT.

It's unclear whether this non-Poissonian distribution is observed because the multiplication process is indeed non-Poissonian or because of the fact that in practise all PMTs are non-ideal. It has been suggested by [24] that an ideal PMT could have multiplication stages which are in fact Poisson distributed but that all practical implementations produced so far yield dynodes which are inhomogeneous, thus producing output which isn't Poisson distributed.

C.3 The normal distribution

Let Z be a continuous random variable. Z is said to be standard normally distributed with mean 0 and variance 1 if the PDF of Z is given by

$$\phi(x) = \frac{1}{\sqrt{2\pi}} e^{-x^2/2} \tag{C.6}$$

and the CDF is given by

$$\Phi(x) = \frac{1}{\sqrt{2\pi}} \int_{-\infty}^{x} e^{-t^2/2} dt \tag{C.7}$$

for a more general normally distributed random variable X with mean μ and variance σ^2 the PDF is given by

$$f(x) = \frac{1}{\sigma\sqrt{2\pi}} e^{-\frac{(x-\mu)^2}{2\sigma^2}} \tag{C.8}$$

and the CDF is given by

$$F(x) = \Phi\left(\frac{x-\mu}{\sigma}\right) \tag{C.9}$$

Note that X can be expressed through Z as

$$X = \mu + \sigma Z \tag{C.10}$$

C.4 Sigmoid functions

A sigmoid function generally refers to a function shaped like an 'S'. The exact nature of the curve varies between different sigmoid functions but they are all well-suited to describe phenomena where censoring occurs in both ends (i.e. for values which lie outside a closed interval). It is therefore possible that some kind of shifted sigmoid function could be appropriate to use when modelling the observed intensity value in an image as a function of exposure since for low and high exposure the intensity will be truncated at the pure noise level (close to 0) and 1 respectively. Sigmoid functions have been used by [11] as the model for a CTF and many authors report estimated CTFs whose curves closely resemble the characteristics of a sigmoid function, see [3] [9]. Examples of sigmoid functions are the error function $\mathrm{erf}(\cdot)$, the arctangent function $\arctan(\cdot)$ and the Gudermannian function $\mathrm{Gd}(\cdot)$, where the Gudermannian function is defined as

$$\mathrm{Gd}(x) = 2 \cdot \arctan(\tanh(x/2)) \tag{C.11}$$

and the error function is defined as

$$\mathrm{erf}(x) = \frac{2}{\sqrt{\pi}} \int_0^x e^{-t^2} dt \tag{C.12}$$